

AD-A198 141

ARo 21261.2-m5

(2)

DTIC FILE COPY

NON-DESTRUCTIVE TESTING USING INFRARED BIREFRINGENCE

FINAL REPORT

A.K. DUTTA, P.K. AJMERA AND B. HUNER

JULY, 1988

U.S. ARMY RESEARCH OFFICE

CONTRACT NO: DAAG29-84-K-0153

LOUISIANA STATE UNIVERSITY
DEPARTMENT OF ELECTRICAL & COMPUTER ENGINEERING
BATON ROUGE, LA 70803

DTIC
ELECTE
AUG 1 2 1988
S H D

APPROVED FOR PUBLIC RELEASE;
DISTRIBUTION UNLIMITED.

THE VIEW, OPINIONS, AND/OR FINDINGS CONTAINED IN THIS REPORT ARE THOSE OF THE AUTHOR(S) AND SHOULD NOT BE CONSTRUED AS AN OFFICIAL DEPARTMENT OF THE ARMY POSITION, POLICY, OR DECISION, UNLESS SO DESIGNATED BY OTHER DOCUMENTATION.

REPORT DOCUMENTATION PAGE

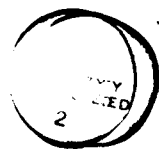
1a. REPORT SECURITY CLASSIFICATION Unclassified		1b. RESTRICTIVE MARKINGS	
2a. SECURITY CLASSIFICATION AUTHORITY		3. DISTRIBUTION/AVAILABILITY OF REPORT Approved for public release; distribution unlimited.	
2b. DECLASSIFICATION/DOWNGRADING SCHEDULE		5. MONITORING ORGANIZATION REPORT NUMBER(S) ARO 21261.2-MS	
4. PERFORMING ORGANIZATION REPORT NUMBER(S)		7a. NAME OF MONITORING ORGANIZATION U. S. Army Research Office	
6a. NAME OF PERFORMING ORGANIZATION Louisiana State University	6b. OFFICE SYMBOL (If applicable)	7b. ADDRESS (City, State, and ZIP Code) P. O. Box 12211 Research Triangle Park, NC 27709-2211	
6c. ADDRESS (City, State, and ZIP Code) Baton Rouge, Louisiana 70803	9. PROCUREMENT INSTRUMENT IDENTIFICATION NUMBER DAA629-84-K-0153		
8a. NAME OF FUNDING/SPONSORING ORGANIZATION U. S. Army Research Office	8b. OFFICE SYMBOL (If applicable)	10. SOURCE OF FUNDING NUMBERS	
8c. ADDRESS (City, State, and ZIP Code) P. O. Box 12211 Research Triangle Park, NC 27709-2211	PROGRAM ELEMENT NO.	PROJECT NO.	TASK NO.
11. TITLE (Include Security Classification) Non-Destructive Testing Using Infrared Birefringence (Unclassified)		WORK UNIT ACCESSION NO.	
12. PERSONAL AUTHOR(S) Dutta, Alope K., Ajmera, Pratul K. and Huner, Burke			
13a. TYPE OF REPORT Final	13b. TIME COVERED FROM 84/8/6 TO 88/2/5	14. DATE OF REPORT (Year, Month, Day) 1988/7/20	15. PAGE COUNT 62
16. SUPPLEMENTARY NOTATION The view, opinions and/or findings contained in this report are those of the author(s) and should not be construed as an official Department of the Army position, policy, or decision, unless so designated by other documentation.			
17. COSATI CODES		18. SUBJECT TERMS (Continue on reverse if necessary and identify by block number)	
FIELD	GROUP	SUB-GROUP	
		Infrared birefringence, defect simulation, semiconductor materials, non-destructive characterization, Silicon, Gallium Arsenide, InGaP.	
19. ABSTRACT (Continue on reverse if necessary and identify by block number)			
<p>In this work, the technique of infrared piezo-birefringence is investigated for characterization of defects in semiconductor materials. As a first step towards simulating defect images, the cases of diametrically loaded discs of Si and GaAs were examined. Simulated images were generated by a computer and were compared with the experimentally obtained ones subjected to the same conditions. The results showed an excellent match between the two cases.</p> <p>The behavior of the stress-optic coefficient C was also investigated in this work. The value of C has been taken to be a constant in earlier works by other investigators. However, our investigations showed that for (100) oriented Si and GaAs discs subjected to diametrical compression, the values of C depended on the position on the sample surface for a given load, and also depended on the orientation of the applied load with respect</p>			
20. DISTRIBUTION/AVAILABILITY OF ABSTRACT <input type="checkbox"/> UNCLASSIFIED/UNLIMITED <input type="checkbox"/> SAME AS RPT. <input type="checkbox"/> DTIC USERS		21. ABSTRACT SECURITY CLASSIFICATION Unclassified	
22a. NAME OF RESPONSIBLE INDIVIDUAL		22b. TELEPHONE (Include Area Code)	22c. OFFICE SYMBOL

UNCLASSIFIED

SECURITY CLASSIFICATION OF THIS PAGE

to the principal crystal directions. No such dependence was found for (111) oriented Si and GaAs discs subjected to diametrical compression, where C can be taken as a constant as expected from the crystal symmetry. The values of C for (100) oriented Si and GaAs discs subjected to diametrical compression ranged from $2.0 \times 10^{-12} \text{ cm}^2/\text{dyne}$ to $3.0 \times 10^{-12} \text{ cm}^2/\text{dyne}$ for Si and from $0.8 \times 10^{-12} \text{ cm}^2/\text{dyne}$ to $2.6 \times 10^{-12} \text{ cm}^2/\text{dyne}$ for GaAs. For (111) oriented Si and GaAs discs subjected to diametrical compression, the values of C were found to be $2.33 \times 10^{-12} \text{ cm}^2/\text{dyne}$ and $1.94 \times 10^{-12} \text{ cm}^2/\text{dyne}$, respectively.

An algorithm was developed for simulation of images of edge and screw dislocations in semiconductors. As a specific example, image simulations are given for both these defects when the dislocation line, the Burgers vector and the direction of the incident light are along the crystal principal axes. For this special case, when the incident light is perpendicular to the Burgers vector, the simulations found distinguishing features between an edge and a screw dislocation. When the polarization angle of the incident light with respect to the dislocation slip plane is 45° , the image of a screw dislocation was found to disappear. Whereas, for the same polarization angle, the image of an edge dislocation was brightest with a four-petal rosette pattern with equal lobes.



Accession For	
NTIS GRA&I	<input checked="" type="checkbox"/>
DTIC TAB	<input type="checkbox"/>
Unannounced	<input type="checkbox"/>
Justification	
By	
Distribution/	
Availability Codes	
Dist	Avail and/or Special
A-1	

UNCLASSIFIED

SECURITY CLASSIFICATION OF THIS PAGE

NON-DESTRUCTIVE TESTING USING INFRARED BIREFRINGENCE

FINAL REPORT

A.K. DUTTA, P.K. AJMERA AND B. HUNER

JULY, 1988

U.S. ARMY RESEARCH OFFICE

CONTRACT NO: DAAG29-84-K-0153

LOUISIANA STATE UNIVERSITY
DEPARTMENT OF ELECTRICAL & COMPUTER ENGINEERING
BATON ROUGE, LA 70803

APPROVED FOR PUBLIC RELEASE;
DISTRIBUTION UNLIMITED.

THE VIEW, OPINIONS, AND/OR FINDINGS CONTAINED IN THIS REPORT ARE THOSE OF THE AUTHOR(S) AND SHOULD NOT BE CONSTRUED AS AN OFFICIAL DEPARTMENT OF THE ARMY POSITION, POLICY, OR DECISION, UNLESS SO DESIGNATED BY OTHER DOCUMENTATION.

SUMMARY

Defects in semiconductors lead to poor reliability and loss of yield of electronic devices fabricated from these materials. Currently, x-ray topography is used to characterize semiconductor wafers. However, the long time needed to characterize each sample by this technique precludes its use for each individual sample. A technique that is fast, accurate, efficient and able to characterize each sample in a reasonable time is, hence, desirable. One such technique utilizing infrared piezo-birefringence is investigated in this work. The technique is based on changes in the refractive index of the material under stress. The stress could be from an applied external load or due to defects in the material generated during its growth and/or processing. The purpose of this research is to investigate the use of infrared birefringence in defect characterization of semiconductor materials.

As a first step towards defect image simulation, the case of diametrically loaded discs of semiconductor materials is examined. This is done to obtain a better understanding of the simulation algorithm prior to its subsequent use in defect characterization. A dark-field plane polariscope was constructed with a He-Ne laser tuned to $1.15\text{ }\mu\text{m}$ wavelength used as the light source. This particular wavelength was selected as the semiconductor materials of primary interest, namely Si and GaAs, are transparent at this wavelength in the near infrared. The computer simulated images matched remarkably well with the experimentally observed ones.

The behavior of the stress-optic coefficient C was also investigated, which has been treated as a constant by other investigators in earlier works. In this work, it was found that for (100) oriented Si and GaAs discs under diametrical compression, the stress-optic coefficient C is a strong function of position for a given load, and also changes with the orientation of the applied load with respect to the principal crystal axes. However, no such dependence was found for (111) oriented Si and GaAs discs under diametrical compression, as expected from the crystal symmetry. The values of C for (100) oriented Si disc under diametrical compression ranged from $2.0 \times 10^{-12}\text{ cm}^2/\text{dyne}$ to $3.0 \times 10^{-12}\text{ cm}^2/\text{dyne}$ and for (100) oriented GaAs disc under diametrical compression ranged from $0.8 \times 10^{-12}\text{ cm}^2/\text{dyne}$ to $2.6 \times 10^{-12}\text{ cm}^2/\text{dyne}$. The corresponding figures for (111) oriented Si and GaAs discs under diametrical compression are $2.33 \times 10^{-12}\text{ cm}^2/\text{dyne}$ and $1.94 \times 10^{-12}\text{ cm}^2/\text{dyne}$, respectively.

Next, an algorithm was developed for simulation of images of edge and screw dislocations in semiconductors. For simplification purposes, image simulations were carried out for edge and screw dislocations when the dislocation line, the Burgers vector and the direction of the incident light were along the crystal principal axes. For this special case when the incident light was perpendicular to the Burgers vector, the computer simulation found distinguishing features between an edge and a screw dislocation. When the polarization angle of the incident light with respect to the dislocation slip plane was 45° , the image of a screw dislocation was found to disappear. Whereas, for the same polarization angle, the image of an edge dislocation was brightest with a four-petal rosette pattern with equal lobes.

An extension of this work is being carried out in our laboratory to generalize the algorithm for screw and edge dislocations to take into account any arbitrary orientation of the dislocation line and the Burgers vector along with any arbitrary direction of the incident light. In principle, a variety of these images for varying polarization angles of the incident light can be generated and stored on a computer. A sample with an unknown defect can be placed under the polariscope and the images monitored for varying incident light polarization angles and its incident directions. Then an image matching procedure can be applied to match the experimentally generated images with the simulated ones stored in the computer. A direct comparison will then give the type of defect, its location, and its orientation with respect to the principal crystal planes.

FOREWORD

This research task was started with Dr. Craig S. Hartley as the project director in August, 1984. However, due to a change in plans, Dr. Hartley left LSU in August, 1986. Since then, the project was carried out under the direction of Dr. Pratul K. Ajmera.

TABLE OF CONTENTS

	Page
Cover Page.....	i
Disclaimer Notice.....	ii
Summary.....	iii
Foreword.....	v
Table of Contents.....	vi
List of Figures.....	vii
List of Tables.....	ix
1. Introduction.....	1
2. Image Simulations.....	3
2.1 Semiconductor Discs under Diametrical Compression.....	3
2.2 Edge Dislocation.....	8
2.3 Screw Dislocation.....	14
3. Results and Discussions.....	21
3.1 Experimental Set-Up.....	21
3.2 Results for Diametrically Compressed Semiconductor Discs....	21
3.3 Stress-Optic Coefficient.....	29
3.4 Simulation Results for Edge and Screw Dislocations.....	33
4. Summary and Conclusions.....	38
5. References.....	40
6. Appendices.....	41
6.1 Direction Cosines for a (100) Plane Under Arbitrary Loading.	41
6.2 Direction Cosines for a (111) Plane Under Arbitrary Loading.	41
6.3 Piezo-Optic Coefficients for Gallium Arsenide from the Elasto-Optic and the Stiffness Coefficients.....	47
Distribution List.....	52

LIST OF FIGURES

Figures	Page
2.1.1 The sample geometry. Axis x_3 is the outward normal from the plane of the paper.	4
2.2.1 Sample with x-z plane as the dislocation slip plane.	10
2.3.1 A right-handed screw dislocation along the axis of a cylinder of radius R and length L.	15
3.1.1 (a) The general view of the experimental set-up. (b) The schematic arrangement of the experimental set-up.	22
3.2.1 (a) Experimentally observed image on a (111) silicon disc of radius 0.873 cm and thickness 0.16 cm. Diametrical compression load $P = 19$ kg, angle of polarization $\alpha = 90^\circ$. (b) Simulated image for the same conditions as (a). Normalized intensity is plotted on a logarithmic scale for the computed image... ..	24
3.2.2 (a) Experimentally observed and (b) computed images on a (111) silicon disc of radius 0.873 cm, thickness 0.16 cm for a load of 38 kg and the angle of polarization α of 90° . Normalized intensity is plotted on a logarithmic scale for the computed image.	25
3.2.3 (a) Experimentally observed image reported by Appel et. al. [11] for a silicon sample of unknown orientation with a radius of 0.437 cm, thickness of 0.188 cm, load of 38 kg and the angle of polarization α of the incident light of 60° , (b) simulated image for the same conditions as (a) for (100) orientation, and (c) same as (b) but for (111) orientation. Normalized intensity is plotted on a logarithmic scale for the computed images.	26
3.2.4 (a) Simulated image on a (100) gallium arsenide disc of radius 0.375 inch and thickness 65 mils. Diametrical compression load $P = 20$ kg, angle of polarization $\alpha = 0^\circ$. (b) Experimentally obtained image for the same conditions as (a). Normalized intensity is plotted on a logarithmic scale for the simulated image.	27
3.2.5 (a) Simulated image on a (100) gallium arsenide disc of radius 0.375 inch and thickness 65 mils. Diametrical compression load $P = 40$ kg, angle of polarization $\alpha = 45^\circ$. (b) Experimentally obtained image for the same conditions as (a). Normalized intensity is plotted on a logarithmic scale for the simulated image.	28

List of Figures (continued)

Figures	Page
3.3.1 Wafer map of the computed values of the stress-optic coefficient C for a) $\delta = 45^\circ$ and b) $\delta = 75^\circ$ for a load of 19 kg, (100) silicon wafer with radius of 0.873 cm and thickness of 0.16 cm. Plotted in 11 levels of gray scale with white for $C > 2.95 \times 10^{-12} \text{ cm}^2/\text{dyne}$ and black for $C < 2.05 \times 10^{-12} \text{ cm}^2/\text{dyne}$	31
3.3.2 Wafer map of the computed values of the stress-optic coefficient C for a) $\delta = 45^\circ$ and b) $\delta = 75^\circ$ for a load of 20 kg, (100) gallium arsenide wafer with radius of 0.375 inch and thickness of 65 mils. Plotted in 10 levels of gray scale with white for $C > 2.5 \times 10^{-12} \text{ cm}^2/\text{dyne}$ and black for $C < 0.9 \times 10^{-12} \text{ cm}^2/\text{dyne}$	32
3.4.1 Simulated fringe patterns for an edge dislocation on a (100) Si surface with the dislocation slip plane along one of the principal crystal plane and the Burger's vector along one of the principal crystal direction. α is the angle between the dislocation slip plane and the polarization axis of the incident light. a) $\alpha = 0^\circ$, b) $\alpha = 30^\circ$, c) $\alpha = 45^\circ$, d) $\alpha = 60^\circ$..	34
3.4.2 Simulated fringe patterns for a screw dislocation on a (100) Si surface with the dislocation slip plane along one of the principal crystal plane and the Burger's vector along one of the principal crystal direction. α is the angle between the dislocation slip plane and the polarization axis of the incident light. a) $\alpha = 0^\circ$, b) $\alpha = 25^\circ$, c) $\alpha = 50^\circ$, d) $\alpha = 75^\circ$...	36
6.1.1 The loading and the crystal principal axes systems for a (100) plane.	42
6.2.1 The loading axes coordinate system.	43
6.2.2 The crystal axes system and its orientation with respect to the plane of the wafer.	43
6.2.3 The (x_1'', x_2'', x_3'') coordinate system and its relationship to the loading axes system and the crystal principal axes system.....	44

LIST OF TABLES

Tables	Page
2.1.1 Conversion technique from tensor to reduced notation.	9
2.1.2 The piezo-optic coefficients for Si used in computation (after [2]).	9
2.1.3 The piezo-optic coefficients of GaAs as derived from data of Booyens and Basson [9].	9
6.3.1 The values of the elasto-optic coefficients (p_{ij}) and the stiffness (c_{ij}) for GaAs after Booyens and Basson [9]. (p_{ij} are dimensionless, c_{ij} are in dyne/cm ²).	51

1. INTRODUCTION

Defects in semiconductor crystals play a major role in the final yield of a manufacturing process, where the yield is defined as the number of good chips on a wafer divided by the total number of chips on the wafer. The defects also have a significant impact on device properties and parameters such as minority carrier lifetime, carrier mobility, carrier generation rate, impurity diffusion, optical properties - such as the index of refraction and the optical absorption spectrum. These factors can lead to poor reliability of the device and low yield. An efficient way of characterizing these defects will not only improve the yield of the manufacturing process, but also improve the device performance.

The most commonly used technique today for defect characterization is X-Ray topography [1]. The theory behind the technique is Bragg's law of diffraction, generalized by Laue. However, the relatively long exposure time needed for characterizing one wafer makes the turn-around time quite long (of the order of 1-2 days). This fact precludes testing each individual sample, and the usability of a lot is determined by statistical estimates. The fact that all the wafers are not tested allows some defective wafers to pass through. Therefore, a technique which is fast, accurate, and efficient, and which can characterize each sample in a reasonable time is likely to improve the yield and device performance. The technique being considered here is infrared piezo-birefringence, which may prove useful in fast and accurate characterization of defects in semiconductor materials.

Most semiconductor crystals such as silicon and gallium arsenide employed for fabricating electronic devices are optically isotropic. Both these materials are opaque to visible light but are transparent in the near infrared. Silicon having a band gap of 1.12 eV has an absorption cutoff at 1.11 μm . The corresponding values for gallium arsenide are 1.42 eV and 0.89 μm , respectively. Light with wavelength longer than 1.11 μm will normally pass through these two materials. The light does not experience any relative phase change while traversing through these optically isotropic samples. Therefore, if a sample is placed between the polarizer and the analyzer with their axes crossed, a dark image will be seen. However, under stress, the sample becomes birefringent. The stress can be applied externally or generated internally due to defects, processing, or material preparation. The light while passing through the stressed regions of the sample splits into two components in mutually orthogonal directions having different refractive indices and thus velocities along the two directions. A phase difference builds up between the two components as they traverse the sample. Now, if the sample is viewed through a crossed polarizer and analyzer set-up, an image will be seen. The image will be characteristic of the phase shift between the two components. For each kind of defect, the stress fields will be different and thus different fringe patterns or images will be seen for different kinds of defects such as an edge dislocation or a screw dislocation. This phenomenon of stress-induced splitting of the refractive index into two components is known as piezo-birefringence.

Giardini [2] studied the phenomenon of birefringence in silicon and obtained the values of its piezo-optic coefficients relating the stresses to the changes in the refractive indices. Lederhandler [3] and Hornstra and

Penning [4] observed residual stresses in silicon by the infrared birefringence method. These stresses were attributed to severe thermal gradients present during crystal growth which resulted in frozen-in strain in the material. Jenkins et.al. [5-6] have studied images of dislocations in silicon samples by the piezo-birefringence method. The stresses produced by the dislocations cause the normally optically isotropic silicon to become birefringent.

In the work carried out here, infrared piezo-birefringence is utilized to examine image patterns obtained by a dark field plane polariscope from infrared transparent semiconductor samples under stress. The normally optically isotropic semiconductor samples become birefringent due to the stress. In this work, image patterns for defects have been simulated on a computer. In some cases, the simulated images are compared to the experimentally observed ones. As a first step to obtain defect images and to obtain a better understanding of the computer image simulation algorithm; images were simulated for externally applied loads on Si and GaAs discs. The experimentally observed and simulated images were compared. Section 2 describes the image simulation algorithms. Subsections 2.1-2.3 discuss the algorithms for semiconductor discs under diametrical compression, edge dislocations, and screw dislocations, respectively.

Section 3 outlines the experimental work done and discussions about the results. Subsection 3.1 gives the experimental set-up utilized in this work. Subsection 3.2 illustrates the results for diametrically compressed semiconductor discs. The experimentally obtained images are compared with the simulated ones. In our work, we investigated the behavior of the stress-optic coefficient C , which was taken to be a constant in earlier works by other investigators. The results of our findings are given in Subsection 3.3. Subsection 3.4 discusses the simulation results for edge and screw dislocations. Section 4 gives the summary of our work along with the conclusions.

2. IMAGE SIMULATIONS

2.1 Semiconductor Discs under Diametrical Compression

In this section, image simulation is carried out for infrared transparent semiconductor discs under externally applied load in the form of diametrical compression. This is done to obtain a better understanding of the simulation algorithm and as a first step towards obtaining simulation images for defects in semiconductors.

The disc under consideration is of radius R , thickness d and under a diametrical compression load P . The loading axes system is defined in Fig.2.1.1. The loading axis x_2 is chosen arbitrarily and does not necessarily coincide with any of the crystal principal axes. Axis x_1 is perpendicular to axis x_2 and lies on the sample surface and axis x_3 is coming out from the plane of the paper. The stress at any point (x_1, x_2) for a disc under diametrical compression is given by [7]

$$\sigma_{11} = -\frac{2P}{\pi d} \left[\frac{(R-x_2)x_1^2}{r_1^4} + \frac{(R+x_2)x_1^2}{r_2^4} - \frac{1}{2R} \right], \quad (2.1.1)$$

$$\sigma_{22} = -\frac{2P}{\pi d} \left[\frac{(R-x_2)^3}{r_1^4} + \frac{(R+x_2)^3}{r_2^4} - \frac{1}{2R} \right], \quad (2.1.2)$$

and

$$\sigma_{12} = \frac{2P}{\pi d} \left[\frac{(R-x_2)^2 x_1}{r_1^4} - \frac{(R+x_2)^2 x_1}{r_2^4} \right] \quad (2.1.3)$$

where $r_1^2 = x_1^2 + (R-x_2)^2$ and $r_2^2 = x_1^2 + (R+x_2)^2$. Here σ_{ij} is the stress produced in direction x_i transmitted across a surface perpendicular to direction x_j . The σ_{11} and σ_{22} components are the normal components of stress while σ_{12} is the shear component with $\sigma_{12} = \sigma_{21}$ because there is no resultant torque in the system. In order to compute the stress components σ_{ij} , the sample is divided into small squares and the stresses are calculated at the center of each of these squares. The semiconductor materials of primary interest in this work are Si and GaAs both of which belong to the cubic class of crystal symmetry. The indicatrix of a cubic crystal under unstressed condition is spherical with no preferred optic axis. However, under stress the indicatrix changes to an ellipsoid of revolution and can be given by a quadric surface [8]

$$\sum_{k, \ell} B_{k\ell} x_k x_\ell = 1 \quad (k=1,2,3; \ell=1,2,3) \quad (2.1.4)$$

where k and ℓ are summation indices and $B_{k\ell}$ are the elements of the dielectric impermeability matrix defined by $B_{k\ell} = B_{k\ell}^0 + \Delta B_{k\ell}$, where $B_{k\ell}^0$ are the elements of the dielectric impermeability tensor. For an isotropic material, the only non-zero values of $B_{k\ell}^0$ are given by $B_{11}^0 = B_{22}^0 = B_{33}^0 = B_0$,

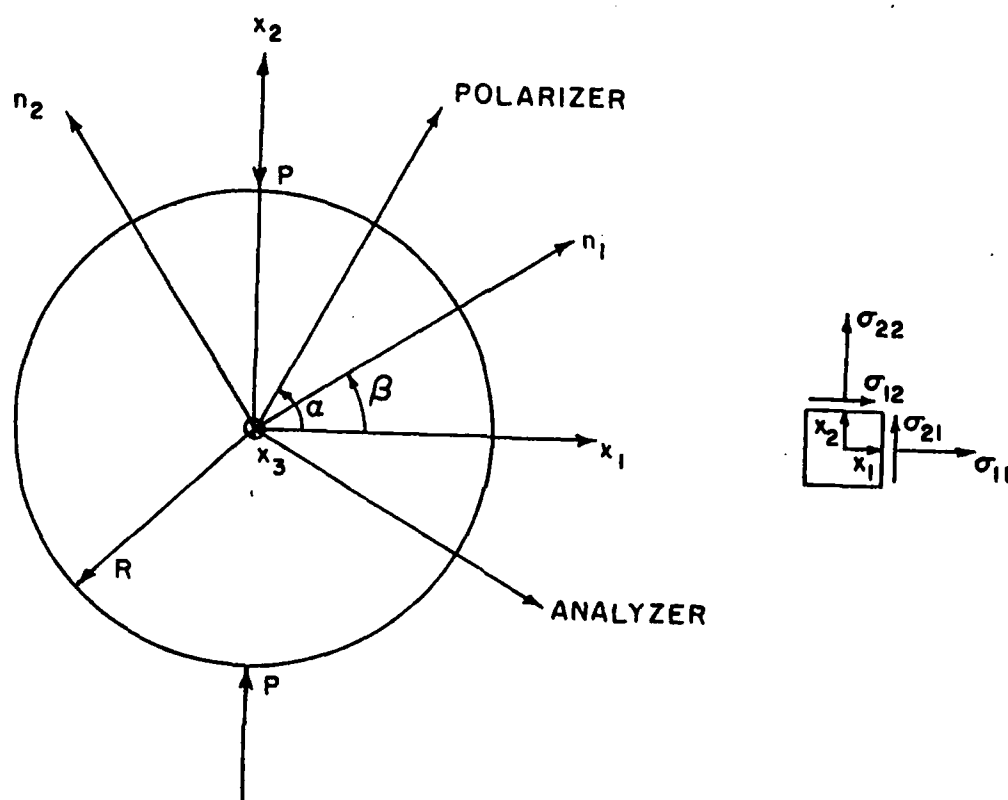


Fig.2.1.1. The sample geometry. Axis x_3 is the outward normal from the plane of the paper.

where $B_0 = \frac{1}{n_0^2}$ and where n_0 is the isotropic value of the refractive index.

Here, ΔB_{kl} are the changes in B_{kl}^0 due to the stress components. When the light is incident along $-x_3$ direction, the intersection ellipse as obtained from Eqn.(2.1.4) is given by:

$$(B_0 + \Delta B_{11})x_1^2 + (B_0 + \Delta B_{22})x_2^2 + \Delta B_{12}x_1x_2 + \Delta B_{21}x_2x_1 = 1. \quad (2.1.5)$$

The diagonalization of Eqn.(2.1.5) would give the major and the minor axes of the ellipse formed by the intersection of the incident light direction with the indicatrix. The result of the diagonalization yields B_1 and B_2 , the dielectric impermeabilities along the minor and the major axes of the index ellipse respectively. They are given as:

$$B_1 = B_0 + \frac{\Delta B_{11} + \Delta B_{22}}{2} + \frac{1}{2} [(\Delta B_{11} - \Delta B_{22})^2 + 4\Delta B_{12}\Delta B_{21}]^{1/2}, \quad (2.1.6)$$

and

$$B_2 = B_0 + \frac{\Delta B_{11} + \Delta B_{22}}{2} - \frac{1}{2} [(\Delta B_{11} - \Delta B_{22})^2 + 4\Delta B_{12}\Delta B_{21}]^{1/2}. \quad (2.1.7)$$

The corresponding refractive indices are given by $n_1 = 1/\sqrt{B_1}$ and $n_2 = 1/\sqrt{B_2}$. Due to these local differences in the refractive indices, the components of a plane polarized light beam traversing the sample will show a phase shift. When the light emerging from the sample is viewed through an analyzer, the resultant image will show a pattern characteristic of this phase shift.

The piezo-optic coefficients π_{ijkl} are used to compute the changes in the dielectric impermeability elements ΔB_{kl} . The piezo-optic coefficients are conventionally defined along the crystal principal axes. Therefore, the computation is carried out in two steps. First, the stress components σ_{ij} obtained from Eqns.(2.1.1-2.1.3) are transformed to the crystal principal axes. Then, the changes in the dielectric impermeability elements are obtained in the crystal principal axes system. These are then converted back to the loading axes system.

The equations for transforming the stress components from the loading axes system (x_1, x_2, x_3) to the crystal principal axes system (x'_1, x'_2, x'_3) are given by [8] as

$$\sigma'_{kl} = \sum_{i,j} a'_{ki} a_{lj} \sigma_{ij} \quad (i=1,2,3; j=1,2,3) \quad (2.1.8)$$

where i and j are summation indices and a_{ki} is the direction cosine between the crystal principal axis x'_k and the loading axis x_i . The calculation of the direction cosines for (100) and (111) oriented samples under arbitrary loading direction are discussed in Appendices 6.1 and 6.2, respectively.

In terms of the piezo-optic coefficients π_{ijkl} , the changes in the dielectric impermeability $\Delta B'_{ij}$ in the crystal principal axes system due to the loading are given by [8] as

$$\Delta B'_{ij} = \sum_{k,l} \pi_{ijkl} \sigma'_{kl} \quad (k=1,2,3; l=1,2,3) \quad (2.1.9)$$

where k and l are summation indices and σ'_{kl} are given by Eqn.(2.1.8). The piezo-optic coefficients π_{ijkl} form a fourth-rank tensor having in general 81 terms. A reduced notation suggested by Nye [8] is often used to express the fourth-rank tensor coefficients as given in Table 2.1.1. The dielectric impermeability elements $\Delta B'_{ij}$ evaluated by Eqn.(2.1.9) are defined along the crystal principal axes. The last step of the procedure is to transform these elements back to the loading axes system, which is given by the transformation [8]

$$\Delta B_{kl} = \sum_{i,j} a_{ik} a_{jl} \Delta B'_{ij} \quad (i=1,2,3; j=1,2,3) \quad (2.1.10)$$

where i and j are summation indices and $\Delta B'_{ij}$ are defined by Eqn.(2.1.9). The impermeability elements ΔB_{kl} which are found from Eqn.(2.1.10) are used in Eqns.(2.1.6) and (2.1.7) to obtain the major and the minor axes of the intersection ellipse formed by the incident light with the indicatrix surface. Once B_1 and B_2 are known, the corresponding refractive indices can be found easily from $n_1 = 1/\sqrt{B_1}$ and $n_2 = 1/\sqrt{B_2}$, where n_1 and n_2 are the refractive indices along the minor and the major axes of the index ellipse, respectively. After the refractive indices are known, the intensity calculation can be carried out as given below.

A light wave after passing through the polarizer and incident upon the sample has the form $A \cos(\omega t - \phi + 2\pi x_3/\lambda)$ where λ is the wavelength, ω is the angular frequency and ϕ is an arbitrary phase angle. The component amplitude along the direction of the minor axis of the index ellipse is given by $A \cos(\alpha - \beta)$. As shown in Fig.2.1.1, α and β are respectively the angles subtended by the incident light polarization direction and the minor axis of the index ellipse with respect to the axis x_1 . The angle β is given by [7]

$$\beta = \frac{1}{2} \tan^{-1} \frac{\Delta B_{12} + \Delta B_{21}}{\Delta B_{11} - \Delta B_{22}} \quad (2.1.11)$$

Similarly, the component amplitude along the major axis direction of the index ellipse is given by $A \sin(\alpha - \beta)$. The light intensity transmitted through the analyzer will be polarized along the analyzer direction. The components along the major and the minor axis directions are further resolved along the polarization and the analyzer directions. Let the component amplitudes $A \cos(\alpha - \beta)$ and $A \sin(\alpha - \beta)$ be denoted by A_1 and A_2 , respectively. Thus, for a ray travelling along the minor axis, the component amplitudes along the polarization and the analyzer directions are given by $A_1 \cos(\alpha - \beta)$ and $A_1 \sin(\alpha - \beta)$, respectively. Similarly, for the ray travelling along the major axis, the component amplitudes along the polarization and the analyzer directions are given by $A_2 \sin(\alpha - \beta)$ and $-A_2 \cos(\alpha - \beta)$, respectively.

The net light amplitude L coming out of the analyzer is, hence, written as

$$L = A \sin(\alpha - \beta) \cos(\alpha - \beta) \cos(\omega t - \phi + 2\pi d / \lambda_1) - A \sin(\alpha - \beta) \cos(\alpha - \beta) \cos(\omega t - \phi + 2\pi d / \lambda_2)$$

where $\lambda_1 = \lambda / n_1$ and $\lambda_2 = \lambda / n_2$ are the wavelengths along the minor and the major axes respectively. The above expression can be written as

$$L = (A/2) \sin 2(\alpha - \beta) [\cos(\omega t - \phi + 2\pi d / \lambda_1) - \cos(\omega t - \phi + 2\pi d / \lambda_2)].$$

Squaring and taking the time average to get the net resultant intensity I coming out of the analyzer, one finally obtains

$$I = L^2 = (A^2/2) \sin^2 2(\alpha - \beta) \sin^2 \{\pi d (1/\lambda_1 - 1/\lambda_2)\}. \quad (2.1.12)$$

In general, for each point on the wafer, the stresses and hence, the angle β and the values for λ_1 and λ_2 will be different. Thus, the resultant intensity image will show dark and bright regions resulting in a fringe pattern. The computer program developed in this work uses the above developed analytical approach to compute the intensity of the light transmitted through a stressed sample. The size of the squares for the stress calculation was selected carefully so that the intensity did not show any abrupt discontinuity. For an idea about the sizes of the squares, it will suffice to say that to simulate the images for a diametrically compressed Si disc of 1.746 cm diameter, the total area was divided into approximately 60,000 squares. Silicon and gallium arsenide, the two main semiconductors of interest in this work belong to the cubic class of crystal symmetry; silicon being a member of $m\bar{3}m$ group, and gallium arsenide being a member of $\bar{4}3m$ group. All crystals having cubic symmetry have only three independent, non-equal, and non-zero piezo-optic coefficients out of a possible total of 81. In reduced notation, these three non-zero coefficients are denoted by π_{11} , π_{12} , and π_{44} [8]. Explicitly they can be expressed as follows:

$$1) \quad \pi_{11} = \pi_{22} = \pi_{33},$$

$$\text{or explicitly as} \quad \pi_{1111} = \pi_{2222} = \pi_{3333}; \quad (2.1.13)$$

$$2) \quad \pi_{44} = \pi_{55} = \pi_{66},$$

$$\begin{aligned} \text{or explicitly as} \quad \pi_{1212} &= \pi_{1221} = \pi_{2121} = \pi_{2112} = \pi_{2323} = \pi_{2332} = \pi_{3232} \\ &= \pi_{3223} = \pi_{3131} = \pi_{3113} = \pi_{1313} = \pi_{1331}; \end{aligned} \quad (2.1.14)$$

$$\text{and} \quad 3) \quad \pi_{12} = \pi_{23} = \pi_{31} = \pi_{13} = \pi_{32} = \pi_{21},$$

$$\text{or explicitly as} \quad \pi_{1122} = \pi_{2233} = \pi_{3311} = \pi_{1133} = \pi_{3322} = \pi_{2211}. \quad (2.1.15)$$

For silicon, the values used in Eqn.(2.1.9) in this program were taken from Giardini [2] and are shown in Table 2.1.2. These values were measured at a wavelength of 1.11 μm by Giardini [2] which is close to the wavelength of 1.15 μm used in this work. For gallium arsenide, to the best of our knowledge, the values for the piezo-optic coefficients are not available in the open literature. However, the paper by Booyens and Basson [9] has reported the elasto-optic coefficients and the stiffness values of gallium arsenide at a wavelength of 1.15 μm . The procedure of obtaining the piezo-optic coefficients from the elasto-optic coefficients and the stiffness values is given in Appendix 6.3 and the calculated values are shown in Table 2.1.3. In the computer program, quadruple precision arithmetic is used throughout to maintain numerical accuracy.

2.2 Edge Dislocation

This section deals with the intensity distribution around a straight edge dislocation viewed by infrared light. The sample is taken to be a square with the slip plane perpendicular to the sample surface. It is assumed that the slip plane makes an angle of ψ with one of the crystal principal axes. In this section, as before, all primed notations refer to the crystal axes system and all unprimed notations refer to the sample axes system. The approach given here is quite general and is demonstrated here for a specific situation. As a specific example, we take a (100) surface of silicon crystal with the dislocation slip plane lying perpendicular to the surface. In this example, we assume that the crystal x' -axis comes out of the plane of the paper and the crystal y' -axis makes an angle of ψ with the dislocation line which is also taken to be the sample x -axis as shown in Fig.2.2.1. This assumption is made to simplify the computations for this example.

The stresses associated with the dislocation are given by the following formulae [10]:

$$\sigma_{11} = \frac{\mu b}{2\pi(1-\nu)} \frac{y(3x^2+y^2)}{(x^2+y^2)^2}, \quad (2.2.1)$$

$$\sigma_{22} = -\frac{\mu b}{2\pi(1-\nu)} \frac{y(x^2-y^2)}{(x^2+y^2)^2}, \quad (2.2.2)$$

$$\sigma_{33} = \nu(\sigma_{11}+\sigma_{22}) = \frac{\mu\nu b y}{\pi(1-\nu)(x^2+y^2)}, \quad (2.2.3)$$

$$\sigma_{12} = -\frac{\mu b}{2\pi(1-\nu)} \frac{x(x^2-y^2)}{(x^2+y^2)^2}, \quad (2.2.4)$$

Table 2.1.1

Conversion technique from tensor to reduced notation.

Tensor notation	11	22	33	23,32	31,13	12,21
Reduced notation	1	2	3	4	5	6

Table 2.1.2

The piezo-optic coefficients for Si used
in computation (after [2]).

Coefficient	Value (cm ² /dyne)
π_{1111}	- 9.0 x 10 ⁻¹⁴
π_{1122}	6.0 x 10 ⁻¹⁴
π_{1212}	- 5.0 x 10 ⁻¹⁴

Table 2.1.3

The piezo-optic coefficients of GaAs as derived
from data of Booyens and Basson [9].

Coefficient	Value (cm ² /dyne)
π_{1111}	- 9.115 x 10 ⁻¹⁴
π_{1122}	- 5.269 x 10 ⁻¹⁴
π_{1212}	- 6.061 x 10 ⁻¹⁴

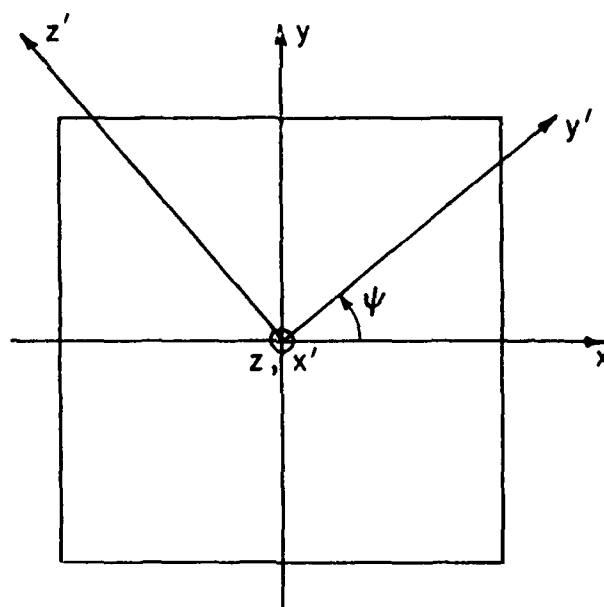


Fig.2.2.1 Sample with x-z plane as the dislocation slip plane.

and

$$\sigma_{13} = \sigma_{23} = 0. \quad (2.2.5)$$

Here, μ is the shear modulus, b is the magnitude of the Burger's vector and ν is the Poisson's ratio. Also, $\sigma_{21} = \sigma_{12}$, and $\sigma_{31} = \sigma_{32} = 0$, as there cannot be any resultant torque in the system.

Next, the direction cosines a_{ij} between the crystal and the sample axes systems are evaluated. These are needed to transform the stress components to the crystal axes system. For the specific example chosen here, they are given by

$$\begin{aligned} a_{11} &= \cos x_1 \hat{x}_1' = \cos x \hat{x}' = \cos 90 = 0, \\ a_{12} &= \cos x_2 \hat{x}_1' = \cos y \hat{x}' = \cos 90 = 0, \\ a_{13} &= \cos x_3 \hat{x}_1' = \cos z \hat{x}' = \cos 0 = 1, \\ a_{21} &= \cos x_1 \hat{x}_2' = \cos x \hat{y}' = \cos \psi, \\ a_{22} &= \cos x_2 \hat{x}_2' = \cos y \hat{y}' = \cos (90-\psi), \\ a_{23} &= \cos x_3 \hat{x}_2' = \cos z \hat{y}' = \cos 90 = 0, \\ a_{31} &= \cos x_1 \hat{x}_3' = \cos x \hat{z}' = \cos (90+\psi), \\ a_{32} &= \cos x_2 \hat{x}_3' = \cos y \hat{z}' = \cos \psi, \\ a_{33} &= \cos x_3 \hat{x}_3' = \cos z \hat{z}' = \cos 90 = 0. \end{aligned} \quad (2.2.6)$$

Once the direction cosines are evaluated, the stress components can be transformed to the crystal axes system through the following transformation:

$$\sigma'_{kl} = \sum_{i,j} a_{ki} a_{lj} \sigma_{ij} \quad (i=1,2,3; j=1,2,3). \quad (2.2.7)$$

Each of the σ'_{kl} term is summed over nine terms. However, $\sigma_{23} = \sigma_{32} = \sigma_{13} = \sigma_{31} = 0$, as well as, $\sigma_{12} = \sigma_{21}$. Taking these into account, Eqn.(2.2.7) simplifies to

$$\sigma'_{kl} = a_{k1} a_{l1} \sigma_{11} + (a_{k1} a_{l2} + a_{k2} a_{l1}) \sigma_{12} + a_{k2} a_{l2} \sigma_{22} + a_{k3} a_{l3} \sigma_{33}. \quad (2.2.8)$$

For the specific case under consideration here for which $a_{11}=a_{12}=a_{23}=a_{33}=0$, and $a_{13} = 1$, Eqn. (2.2.8) can be given by

$$\sigma'_{11} = \sigma_{33},$$

$$\sigma'_{12} = \sigma'_{13} = \sigma'_{21} = \sigma'_{31} = 0,$$

$$\sigma'_{22} = a_{21}^2 \sigma_{11} + 2a_{21}a_{22}\sigma_{12} + a_{22}^2 \sigma_{22},$$

$$\sigma'_{23} = \sigma'_{32} = a_{21}a_{31}\sigma_{11} + (a_{21}a_{32} + a_{22}a_{31})\sigma_{12} + a_{32}a_{22}\sigma_{22},$$

and

$$\sigma'_{33} = a_{31}^2 \sigma_{11} + 2a_{32}a_{31}\sigma_{12} + a_{32}^2 \sigma_{22}. \quad (2.2.9)$$

The changes in the dielectric impermeability tensor elements $\Delta B'_{ij}$ can be calculated from the formula

$$\Delta B'_{ij} = \sum_{k,l} \pi_{ijkl} \sigma'_{kl} \quad (k=1,2,3; l=1,2,3). \quad (2.2.10)$$

The cubic crystal symmetry results in only three independent values of the piezo-optic coefficients π_{ijkl} as given by Eqns.(2.1.13-2.1.15). Taking this into account, the coefficients in Eqn.(2.2.10) can be written as

$$\Delta B'_{11} = \pi_{1111}\sigma'_{11} + \pi_{1122}\sigma'_{22} + \pi_{1133}\sigma'_{33},$$

$$\Delta B'_{12} = B'_{13} = \Delta B'_{21} = \Delta B'_{31} = 0,$$

$$\Delta B'_{22} = \pi_{2222}\sigma'_{22} + \pi_{2211}\sigma'_{11} + \pi_{2233}\sigma'_{33},$$

$$\Delta B'_{23} = \Delta B'_{32} = \pi_{2323}\sigma'_{23} + \pi_{2332}\sigma'_{32},$$

and

$$\Delta B'_{33} = \pi_{3333}\sigma'_{33} + \pi_{3311}\sigma'_{11} + \pi_{3322}\sigma'_{22}. \quad (2.2.11)$$

These dielectric impermeability tensor elements are defined along the crystal axes. These are transformed back to the sample axes through the following transformation

$$\Delta B_{kl} = \sum_{i,j} a_{ik} a_{jl} \Delta B'_{ij} \quad (i=1,2,3; j=1,2,3). \quad (2.2.12)$$

Each of the ΔB_{kl} term is summed over nine terms. Substituting Eqns.(2.2.11) and (2.2.6) in the above equation yields

$$\Delta B_{11} = a_{21}^2 \Delta B'_{22} + 2a_{21}a_{31} \Delta B'_{23} + a_{31}^2 \Delta B'_{33},$$

$$\Delta B_{12} = \Delta B_{21} = a_{21}a_{22} \Delta B'_{22} + a_{21}a_{32} \Delta B'_{23} + a_{31}a_{22} \Delta B'_{32} + a_{31}a_{32} \Delta B'_{33},$$

$$\Delta B_{13} = \Delta B_{31} = \Delta B_{23} = \Delta B_{32} = 0,$$

$$\Delta B_{22} = a_{22}^2 \Delta B'_{22} + 2a_{22}a_{32} \Delta B'_{23} + a_{32}^2 \Delta B'_{33},$$

and

$$\Delta B_{33} = a_{13}^2 \Delta B'_{11}. \quad (2.2.13)$$

The dielectric impermeability matrix now needs to be diagonalized in order to obtain the major and the minor axes of the cross-sectional ellipse formed by the plane perpendicular to the incident light as it cuts the indicatrix. The equation of a quadric surface which denotes the indicatrix is given by

$$\sum_{k,l} B_{kl} x_k x_l = 1 \quad (k=1,2,3; l=1,2,3) \quad (2.2.14)$$

where, as before, $B_{kl} = B_{kl}^0 + \Delta B_{kl}$, and x_1 , x_2 , and x_3 form the rectilinear coordinate system x , y , and z for the sample. B_0 is the isotropic dielectric impermeability, given by $B_0 = 1/n_0^2$ where n_0 is the isotropic refractive index.

As before, the problem can be simplified by taking the ray direction to be parallel to axis $-x_3$ (i.e., along the sample $-z$ axis). In that case, intersection of the plane perpendicular to the ray direction is obtained by setting $x_3 = 0$ and Eqn.(2.2.14) simplifies to give the cross-section of the indicatrix perpendicular to the ray direction as

$$(B_0 + \Delta B_{11})x_1^2 + (B_0 + \Delta B_{22})x_2^2 + \Delta B_{12}x_1x_2 + \Delta B_{21}x_2x_1 = 1. \quad (2.2.15)$$

Forming the matrix, diagonalizing it and solving the characteristic equation, we find the two roots which are given by:

$$B_1 = B_0 + \frac{\Delta B_{11} + \Delta B_{22}}{2} + \frac{1}{2} \left[(\Delta B_{11} - \Delta B_{22})^2 + 4\Delta B_{12}\Delta B_{21} \right]^{1/2}, \quad (2.2.16)$$

and

$$B_2 = B_0 + \frac{\Delta B_{11} + \Delta B_{22}}{2} - \frac{1}{2} \left[(\Delta B_{11} - \Delta B_{22})^2 + 4\Delta B_{12}\Delta B_{21} \right]^{1/2}, \quad (2.2.17)$$

where B_1 and B_2 are the dielectric impermeabilities along the minor and the major axes of the index ellipse, respectively. Once they are known, the refractive indices along those two directions can be easily calculated from $n_1 = 1/\sqrt{B_1}$, and $n_2 = 1/\sqrt{B_2}$.

The image intensity distribution for an edge dislocation can be obtained by following exactly the same procedure taken to calculate the intensity distribution for a semiconductor disc under diametrical compression in Section 2.1. The final expression for the intensity I will be the same as Eqn.(2.1.12) and is rewritten below for convenience.

$$I = (A^2/2) \sin^2 2(\alpha - \beta) \sin^2 \{ \pi d (1/\lambda_1 - 1/\lambda_2) \} \quad (2.2.18)$$

where A is the amplitude of the incident wave, α is the angle the polarizer makes with respect to the sample x-axis, β is the angle given by

$$\beta = \frac{1}{2} \tan^{-1} \frac{\Delta B_{12} + \Delta B_{21}}{\Delta B_{11} - \Delta B_{22}}, \quad (2.2.19)$$

d is the sample thickness, $\lambda_1 = \lambda/n_1$, $\lambda_2 = \lambda/n_2$, and λ is the wavelength of the incident light in vacuum.

It is important to point out here that the approach taken here to obtain the image intensity is quite general. One will need to obtain the values for appropriate coefficients a_{ij} in Eqn.(2.2.6) for other orientations of the edge dislocation. The problem is considerably more tedious if the incident light is not taken to be along the sample z axis.

2.3 Screw Dislocation

In this section, an example of image simulation for screw dislocation is presented. The analysis given in Hirth and Lothe [10] is followed closely. Let us consider a right-handed screw dislocation along the axis of a cylinder of radius R and length L , as shown in Fig.2.3.1. This dislocation can be produced from a perfect cylinder by shear displacements in the z direction.

This dislocation has a Burger's vector \bar{b} with the displacements given by u_1 , u_2 , and u_3 along directions x , y , and z , respectively. The latter directions are also referred to as x_1 , x_2 , and x_3 . The strains and stresses are given by ϵ_{ij} and σ_{ij} , respectively, where both i and j take the values 1, 2, and 3. As is evident from this figure, $u_1 = u_2 = 0$, and the displacement u_3 discontinuous at the cut surface defined by $y = 0$, $x > 0$ is given by

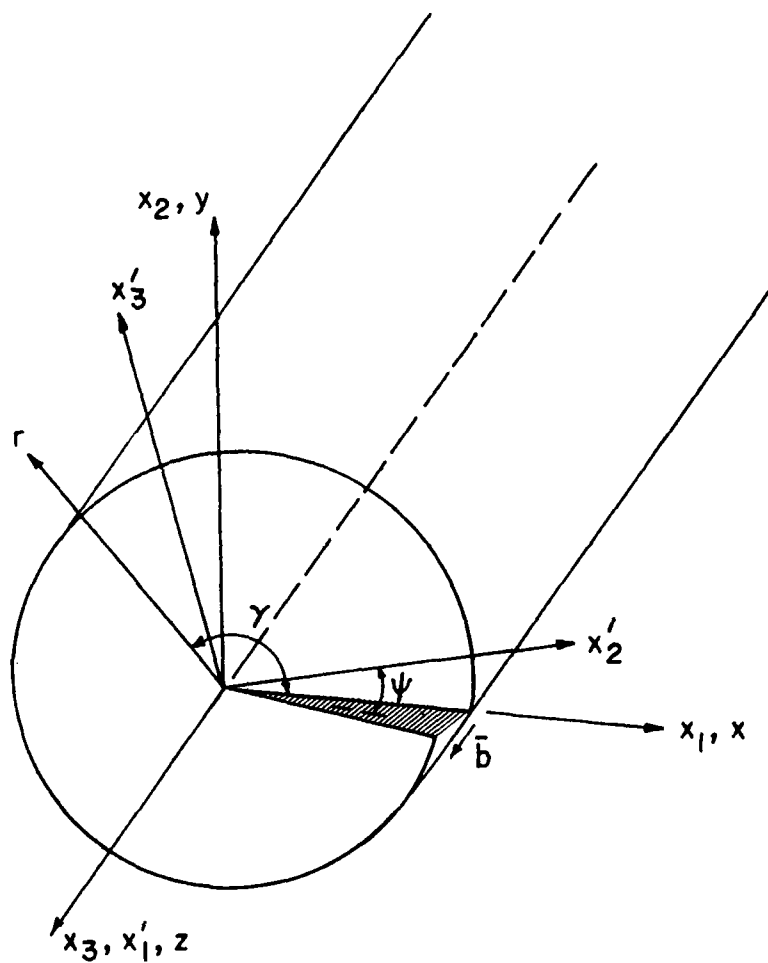


Fig.2.3.1 A right-handed screw dislocation along the axis of a cylinder of radius R and length L .

$$\lim_{\Delta y \rightarrow 0} u_3(x, -\Delta y) - u_3(x, \Delta y) = b \quad (\text{in } z \text{ direction}); \quad \Delta y \text{ positive} \\ x > 0.$$

Assuming that in an isotropic medium the displacement u_3 increases uniformly with the angle γ to give the discontinuity represented in the cylindrical coordinate system as

$$u_3(r, \gamma) = b \frac{\gamma}{2\pi} = \frac{b}{2\pi} \tan^{-1} \frac{y}{x} = \frac{b}{2\pi} \tan^{-1} \frac{x_2}{x_1}. \quad (2.3.1)$$

Now the strains ϵ_{ij} are defined by

$$\epsilon_{ij} = \frac{1}{2} \left\{ \frac{\partial u_i}{\partial x_j} + \frac{\partial u_j}{\partial x_i} \right\} \quad (i=1,2,3; j=1,2,3), \quad (2.3.2)$$

which gives

$$\epsilon_{11} = \epsilon_{22} = \epsilon_{33} = \epsilon_{12} = \epsilon_{21} = 0, \\ \epsilon_{23} = \epsilon_{32} = \frac{b}{4\pi} \frac{\partial}{\partial x_2} \left\{ \tan^{-1} \frac{x_2}{x_1} \right\} = \frac{b}{4\pi} \frac{x_1}{x_1^2 + x_2^2},$$

and

$$\epsilon_{31} = \epsilon_{13} = \frac{b}{4\pi} \frac{\partial}{\partial x_1} \left\{ \tan^{-1} \frac{x_2}{x_1} \right\} = -\frac{b}{4\pi} \frac{x_2}{x_1^2 + x_2^2}. \quad (2.3.3)$$

The stresses and strains are related by the stiffness coefficients c_{ijkl} . Conventionally these stiffness coefficients are defined only along the crystal principal axes. However, the strain elements ϵ_{ij} in Eqn.(2.3.2) need not be along the crystal principal axes. The axes system chosen to represent the strains due to the screw dislocation, i.e. (x_1, x_2, x_3) need not coincide with any of the principal crystal axes. Subsequently in this section, all primed notations refer to the crystal axes system and all unprimed notations refer to the sample axes system.

The approach can be quite general to take into account any orientation of the slip plane with respect to the crystal principal axes. As a specific example, let us assume the sample to be of (100) orientation, with the crystal x'_1 axis coming out from the sample surface (i.e. along the sample

axis x_3), and the crystal x'_2 axis making an angle of ψ with the dislocation slip plane (i.e. sample x_1x_3 plane) as shown in Fig.2.3.1. For this case, the direction cosines a_{ij} between the crystal axes and the sample axes can be obtained from Eqns.(2.2.6). Once the direction cosines are evaluated, the strains can be converted from the sample axes to the crystal axes by the following transformation

$$\epsilon'_{kl} = \sum_{i,j} a_{ki} a_{lj} \epsilon_{ij} \quad (i=1,2,3; j=1,2,3), \quad (2.3.4)$$

where ϵ'_{kl} give the strain values in the crystal axes system. Each of the ϵ'_{kl} term is summed over nine terms. However, $\epsilon_{11} = \epsilon_{22} = \epsilon_{33} = \epsilon_{12} = \epsilon_{21} = 0$, as well as $\epsilon_{23} = \epsilon_{32}$, and $\epsilon_{31} = \epsilon_{13}$. Taking these into account, Eqn.(2.3.4) can be rewritten as

$$\epsilon'_{kl} = (a_{k1} a_{l3} + a_{k3} a_{l1}) \epsilon_{31} + (a_{k2} a_{l3} + a_{k3} a_{l2}) \epsilon_{23}. \quad (2.3.5)$$

For the specific case under consideration for which the direction cosines are given by Eqns.(2.2.6), we have $a_{11}=a_{12}=a_{23}=a_{33} = 0$, and $a_{13}=1$, and thus Eqn.(2.3.5) can be given by

$$\epsilon'_{11} = \epsilon'_{22} = \epsilon'_{23} = \epsilon'_{32} = \epsilon'_{33} = 0,$$

$$\epsilon'_{12} = \epsilon'_{21} = a_{21} \epsilon_{31} + a_{22} \epsilon_{23},$$

and

$$\epsilon'_{13} = \epsilon'_{31} = a_{31} \epsilon_{31} + a_{32} \epsilon_{23}. \quad (2.3.6)$$

Now the stress components σ'_{ij} along the crystal principal axes can be evaluated by the following equation

$$\sigma'_{ij} = \sum_{k,l} c_{ijkl} \epsilon'_{kl} \quad (k=1,2,3; l=1,2,3), \quad (2.3.7)$$

where ϵ'_{kl} are defined by Eqn.(2.3.6). The stiffness coefficients c_{ijkl} used in Eqn.(2.3.7) can be expressed in reduced notation as done earlier for π_{ijkl} in Eqns.(2.1.13-2.1.15) as

$$c_{ijkl} = c_{mn} \quad (i,j,k,l=1,2,3; m,n=1,2,\dots,6). \quad (2.3.8)$$

As before for materials with cubic $\bar{4}3m$ or $m3m$ symmetry, the following equalities are valid:

$$c_{11} = c_{22} = c_{33},$$

$$\text{i.e., } c_{1111} = c_{2222} = c_{3333};$$

$$c_{12} = c_{21} = c_{13} = c_{31} = c_{23} = c_{32},$$

$$\text{i.e., } c_{1122} = c_{2211} = c_{1133} = c_{3311} = c_{2233} = c_{3322};$$

$$c_{44} = c_{55} = c_{66},$$

$$\text{i.e., } c_{2332} = c_{2323} = c_{3223} = c_{3232} = c_{3113} = c_{3131}$$

$$= c_{1331} = c_{1313} = c_{1212} = c_{2121} = c_{1221} = c_{2112};$$

and

$$c_{14} = c_{15} = c_{16} = c_{24} = c_{25} = c_{26} = c_{34} = c_{35} = c_{36} = c_{41} = c_{42} = c_{43}$$

$$= c_{45} = c_{46} = c_{51} = c_{52} = c_{53} = c_{54} = c_{56} = c_{61} = c_{62} = c_{63} = c_{64} = c_{65} = 0;$$

as there are only three non-equal stiffness constants namely, c_{11} , c_{12} , and c_{44} . Substituting the above in Eqn.(2.3.7) yields

$$\sigma'_{11} = \sigma'_{22} = \sigma'_{23} = \sigma'_{32} = \sigma'_{33} = 0,$$

$$\sigma'_{12} = \sigma'_{21} = (c_{1212} + c_{1221})\epsilon'_{12} = 2c_{44}\epsilon'_{12},$$

and

$$\sigma'_{13} = \sigma'_{31} = (c_{1313} + c_{1331})\epsilon'_{31} = 2c_{44}\epsilon'_{31}. \quad (2.3.9)$$

However, c_{44} is the shear modulus μ . Therefore,

$$\sigma'_{12} = \sigma'_{21} = 2\mu\epsilon'_{12},$$

and similarly,

$$\sigma'_{31} = \sigma'_{13} = 2\mu\epsilon'_{31}.$$

Once the stress components σ'_{ij} are known, the changes in the dielectric impermeability can be evaluated as done earlier from

$$\Delta B'_{kl} = \sum_{i,j} \pi_{kl ij} \sigma'_{ij} \quad (i=1,2,3; j=1,2,3), \quad (2.3.10)$$

where $\pi_{k\ell ij}$ are the piezo-optic coefficients given earlier in Eqns.(2.1.13-2.1.15). Substitution yields,

$$\Delta B'_{11} = \Delta B'_{22} = \Delta B'_{23} = \Delta B'_{32} = \Delta B'_{33} = 0,$$

$$\Delta B'_{12} = \Delta B'_{21} = 2\pi_{1212}\sigma'_{12},$$

and

$$\Delta B'_{31} = \Delta B'_{13} = 2\pi_{1313}\sigma'_{31}. \quad (2.3.11)$$

These changes in the dielectric impermeability are defined along the crystal principal axes. Now they need to be transferred to the sample axes system through the following transformation

$$\Delta B_{ij} = \sum_{k,\ell} a_{ki}a_{\ell j}\Delta B'_{k\ell} \quad (k=1,2,3; \ell=1,2,3). \quad (2.3.12)$$

Substitution of the values for $\Delta B'_{k\ell}$ from Eqn.(2.3.11) and a_{ij} from Eqn.(2.2.6) into Eqn.(2.3.12) yields

$$\Delta B_{11} = \Delta B_{12} = \Delta B_{21} = \Delta B_{22} = \Delta B_{33} = 0,$$

$$\Delta B_{13} = \Delta B_{31} = a_{21}\Delta B'_{12} + a_{31}\Delta B'_{31},$$

and

$$\Delta B_{23} = \Delta B_{32} = a_{22}\Delta B'_{12} + a_{32}\Delta B'_{31}. \quad (2.3.13)$$

The indicatrix is given by

$$\sum_{i,j} B_{ij}x_i x_j = 1 \quad (i=1,2,3; j=1,2,3). \quad (2.3.14)$$

Expanding as before and remembering that there are no cross-terms under unstressed condition, one obtains

$$(B_0 + \Delta B_{11})x_1^2 + (B_0 + \Delta B_{22})x_2^2 + (B_0 + \Delta B_{33})x_3^2 \\ + 2\Delta B_{12}x_1x_2 + 2\Delta B_{23}x_2x_3 + 2\Delta B_{31}x_3x_1 = 1,$$

or,

$$B_0x_1^2 + B_0x_2^2 + B_0x_3^2 + 2\Delta B_{23}x_2x_3 + 2\Delta B_{31}x_3x_1 = 1. \quad (2.3.15)$$

If the light is incident along the $-x_3$ direction, then the cross-section found by putting $x_3 = 0$ in the above equation gives

$$B_0x_1^2 + B_0x_2^2 = 1, \quad (2.3.16)$$

and there is no birefringence as the cross-section is a circle. Therefore, an important observation is that screw dislocations cannot be viewed end-on, i.e., along the direction of the Burger's vector. However, if the light traverses along other directions, one should be able to see interference fringe patterns due to birefringence. Assuming the light to be falling along the $-x_1$ direction, the cross-section found by putting $x_1 = 0$ in Eqn.(2.3.15) gives

$$B_0 x_2^2 + B_0 x_3^2 + 2\Delta B_{23} x_2 x_3 = 1. \quad (2.3.17)$$

This cross-section is an ellipse and one should see birefringence corresponding to the relative dielectric impermeabilities along the minor and the major axes given by

$$B_1 = B_0 + \Delta B_{23}, \text{ and } B_2 = B_0 - \Delta B_{23}$$

where ΔB_{23} is given by Eqn.(2.3.13), with corresponding refractive indices along its minor axis being $n_1 = 1/\sqrt{B_1}$ and along its major axis being $n_2 = 1/\sqrt{B_2}$. The angle β subtended by the minor index axis with axis x_3 is given by

$$\beta = \frac{1}{2} \tan^{-1} \frac{2\Delta B_{23}}{\Delta B_{33} - \Delta B_{22}}. \quad (2.3.18)$$

However, $\Delta B_{22} = \Delta B_{33} = 0$ and Eqn.(2.3.18) gives the value of β as

$$\beta = \frac{1}{2} \tan^{-1} \infty = \frac{\pi}{4}.$$

As before, the resultant transmitted intensity through the analyzer is given by

$$I = (A^2/2) \sin^2 2(\alpha - \beta) \sin^2 \{ \pi d (1/\lambda_1 - 1/\lambda_2) \} \quad (2.3.19)$$

where $\lambda_1 = \lambda/n_1$, $\lambda_2 = \lambda/n_2$ and λ is the incident light wavelength in vacuum. Here, α is the polarization angle of the incident light measured with respect to the axis x_3 , and d is the material thickness along x_1 direction.

3. RESULTS AND DISCUSSIONS

3.1 Experimental Set-Up

A dark field plane polariscope was constructed to view the fringe patterns of diametrically loaded discs of silicon and gallium arsenide. The setup is shown in Fig.3.1.1. Figure 3.1.1(a) shows a general view of the set-up while Fig.3.1.1(b) shows the schematic arrangement. The light source used was a linearly polarized 19-mW He-Ne laser (Jodon HN-50) tuned to 1.15 μm wavelength. Both silicon and gallium arsenide with absorption cut-off wavelengths of 1.11 μm and 0.89 μm , respectively, are transparent at 1.15 μm wavelength. A Hamamatsu infrared camera (model C-1000-03) was used as a detector. The power output of the laser was strong enough for the detector to pick up bright images. The laser beam was spatially filtered and then expanded to a diameter of 2.5 cm by a combination spatial filter - beam expander arrangement.

A laser light source was selected over the more conventional filtered incoherent light sources because of its monochromaticity. The use of the laser as the source of illumination proved to reduce the washing out effect observed in images formed with wider bandwidth sources. A comparison of Figs.3.2.1(a) and 3.2.2(a) with Fig.3.2.3(a), which is reproduced here from the reported work of Appel et.al. [11], clearly shows improved contrast in the first two cases using a laser light source. An unfortunate artifact of the use of the laser is the production of speckle in the images. This can be seen in Figs.3.2.1(a) and 3.2.2(a) as an overall graininess in the images.

In theory at least the use of the polarized laser beam would have precluded the need for using a polarizer ahead of the sample. However, even in the beam expanded state, the laser source proved to be too powerful and blinded the infrared sensitive camera. Because of the need to rotate the plane of polarization of the light source, and also the need to reduce the light intensity, a polarizer was inserted into the optical path ahead of the sample.

Figures 3.2.1(a) and 3.2.2(a) were photographed directly from the screen of the monitor with a 35-mm camera. The samples were placed between the polarizer and the analyzer and loaded by a pneumatically operated piston. The anvils of the compressor were made of flame-hardened mild steel and pieces of index card were used to protect the edges of the samples during compression. The cross-section of the piston plunger was 1 sq. in. \pm 1%. A pressure gauge calibrated in psig then allowed the compressive force on the sample disc to be read directly.

3.2 Results for Diametrically Compressed Semiconductor Discs

The silicon samples used in this experiment were cut along the (111) orientation from a rod of single crystal silicon of 1.746 cm diameter. To prevent loss of intensity due to surface scattering, the sample surfaces were polished to a mirror finish. The polishing was done manually on both sides of the samples with SiC powder on a glass plate with light hand pressure, using a successively finer abrasive medium starting with 200-grit powder size and ending with 1200 grit powder size. After the mechanical polishing was completed, the samples were chemically polished for 2 min in CP-4A solution containing three parts HF, five parts HNO_3 , and three parts CH_3COOH by volume.

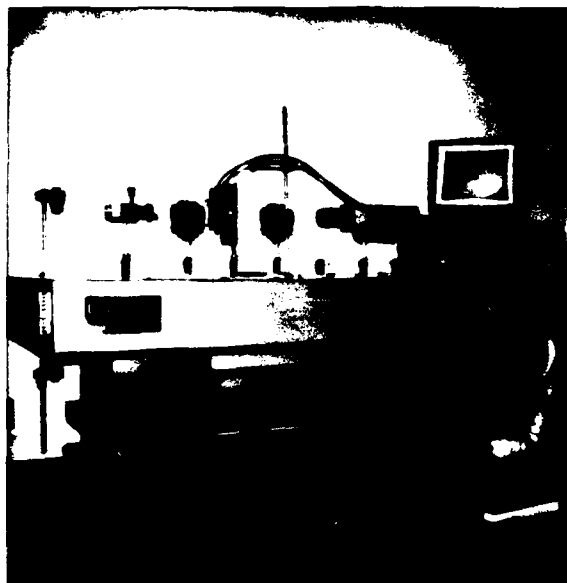


Fig.3.1.1(a) The general view of the experimental set-up.

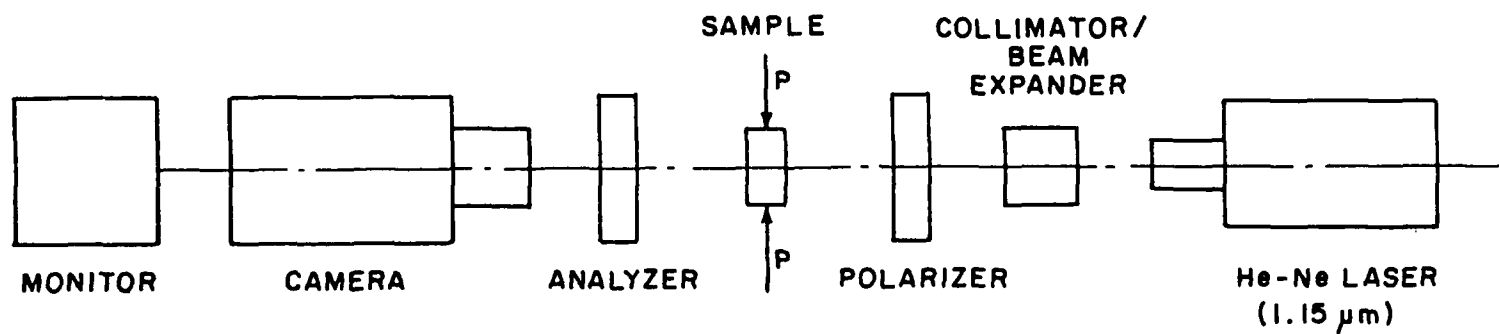


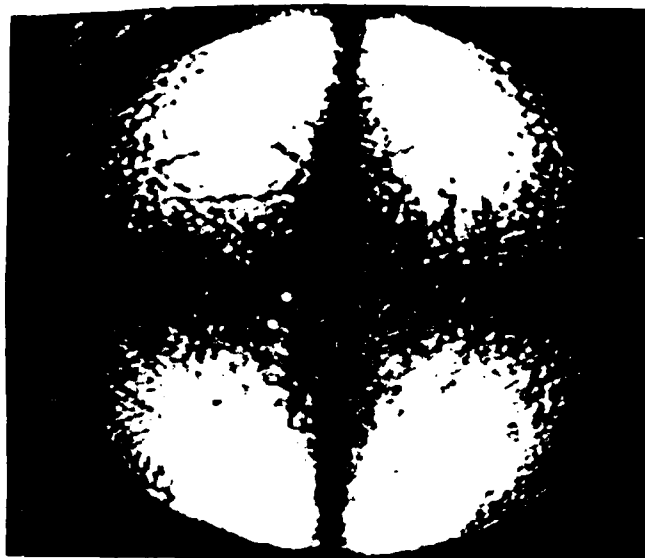
Fig.3.1.1(b) The schematic arrangement of the experimental set-up.

Figure 3.2.1(a) shows the observed image at $1.15\ \mu\text{m}$ under the plane polariscope for a (111) orientation silicon crystal disc of $0.873\ \text{cm}$ radius and $0.16\ \text{cm}$ thickness. The applied load was $19\ \text{kg}$ and the angle of polarization α of the incident light was 90° . Figure 3.2.1(b) is the simulated image for these same conditions obtained from the analysis given in Section 2.1. The intensity levels shown in Fig.3.2.1(b) were obtained by normalizing the maximum level to unity and then plotting in sixteen gray scale levels utilizing a logarithmic scale. Any intensity more than 0.1 in the normalized scale is plotted as white in the computed figure. Figure 3.2.2 compares the observed and the simulated images for the same conditions as Fig.3.2.1 but with the load now increased to $38\ \text{kg}$. A close observation of the simulated image of Fig.3.2.2 will bring out the feature of the small lobes around the point of loading which is also present in the experimentally observed image. Thus the match between the computer simulations and the experimentally observed images is excellent.

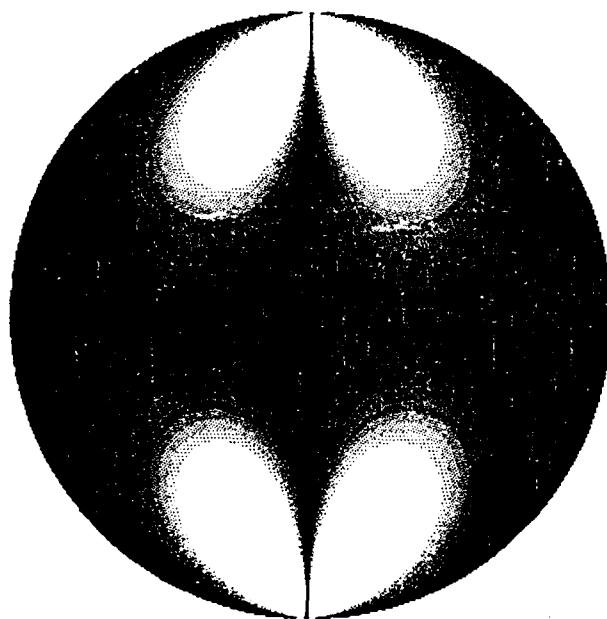
The data reported by Appel et.al. [11] of a silicon sample with radius $R = 0.437\ \text{cm}$, thickness $d = 0.188\ \text{cm}$, and the polarization angle $\alpha = 60^\circ$ are shown in Fig.3.2.3(a). The crystal orientation of the sample was not mentioned in their paper. In this work, we simulated their image by assuming the sample orientation to be (100) and (111). The results of our simulation are shown in Figs.3.2.3(b) and 3.2.3(c), respectively, for (100) and (111) oriented silicon samples. All other parameters used in our simulation were the same as those reported by Appel et.al. [11]. Comparing Fig.3.2.3(a) with Figs.3.2.3(b) and 3.2.3(c), an excellent match is seen between the simulated image and the experimentally observed image for a (100) orientation sample, whereas the simulated image for a (111) orientation sample shows a poor match with the experimental one. The best match for the (100) orientation simulation was obtained for the case in which the load was applied along one of the crystal principal axes. Hence, we infer that the sample used in the work reported by Appel et.al. [11] was of (100) orientation.

Hence, the algorithm can not only be used to predict the interference fringe pattern for any arbitrarily applied stress direction, but can also be used to predict the orientation of an unknown sample by putting it under a compressive load and then by comparing the resulting fringe pattern with the simulated ones.

The algorithm was also used to determine the fringe patterns for a diametrically loaded GaAs disc. The disc was single crystal undoped semi-insulating GaAs of (100) orientation, grown by the Liquid Encapsulated Czochralski (LEC) technique. It was of diameter $0.75\ \text{inch}$ and thickness $65\ \text{mils.}$ Both its surfaces were polished to a mirror finish. Figure 3.2.4(a) shows the simulated pattern for the above disc under a diametrical compression load of $20\ \text{kg}$, and the angle of polarization α of the incident light of 0° . Figure 3.2.4(b) shows the experimentally obtained image for the disc subjected to same conditions as in Fig.3.2.4(a). Figures 3.2.5(a) and 3.2.5(b) show the simulated pattern and the experimentally obtained image of the same disc but with the load now increased to $40\ \text{kg}$ and the angle of polarization α of the incident light changed to 45° . The match between the simulated patterns and the experimentally obtained images confirms the general nature of the algorithm which can effectively be used for a variety of materials.

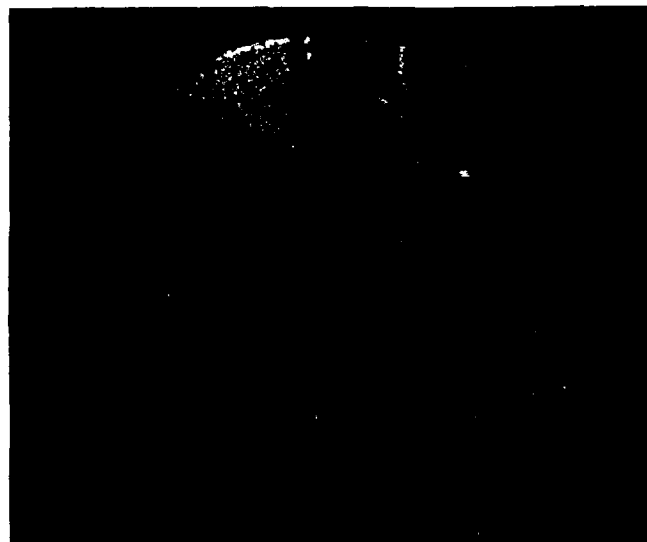


(a)

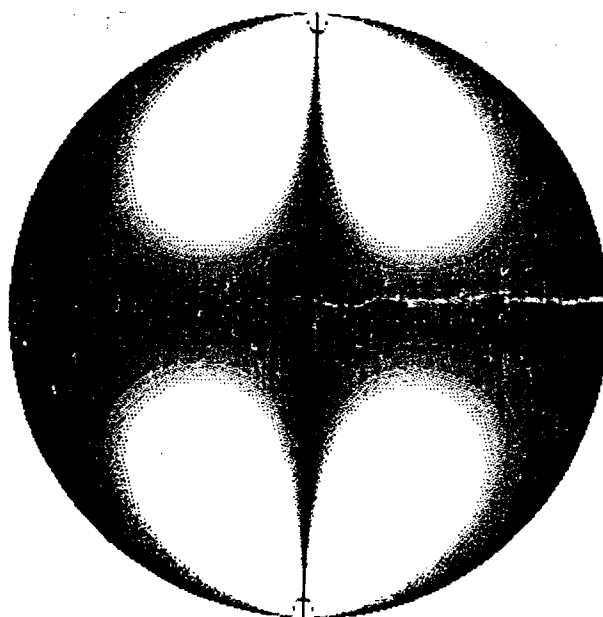


(b)

Fig. 3.2.1. a) Experimentally observed image on a (111) silicon disc of radius 0.873 cm and thickness 0.16 cm. Diametrical compression load $P = 19$ kg, angle of polarization $\alpha = 90^\circ$. b) Simulated image for the same conditions as a). Normalized intensity is plotted on a logarithmic scale for the computed image.

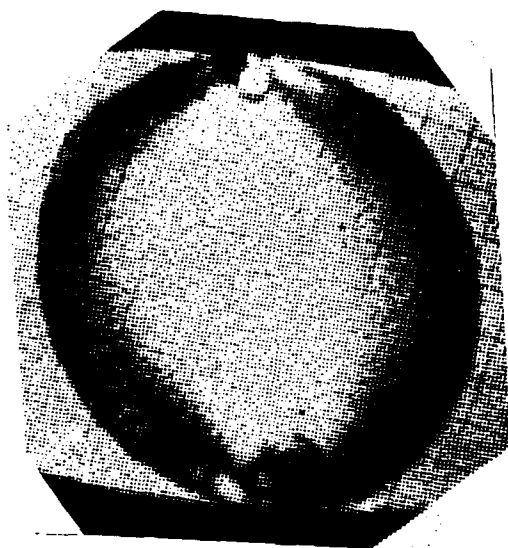


(a)

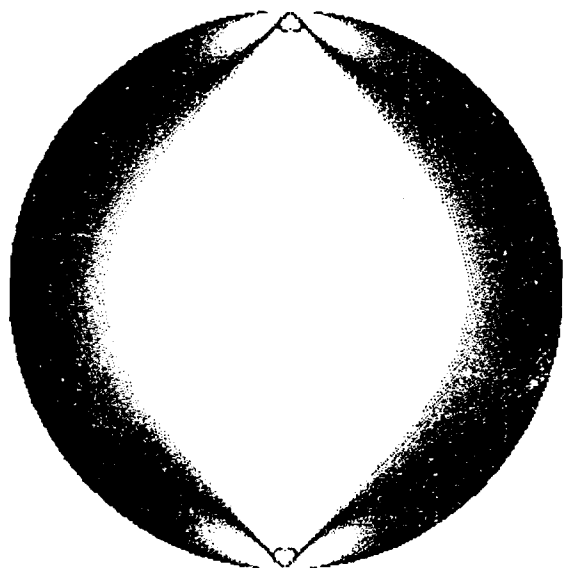


(b)

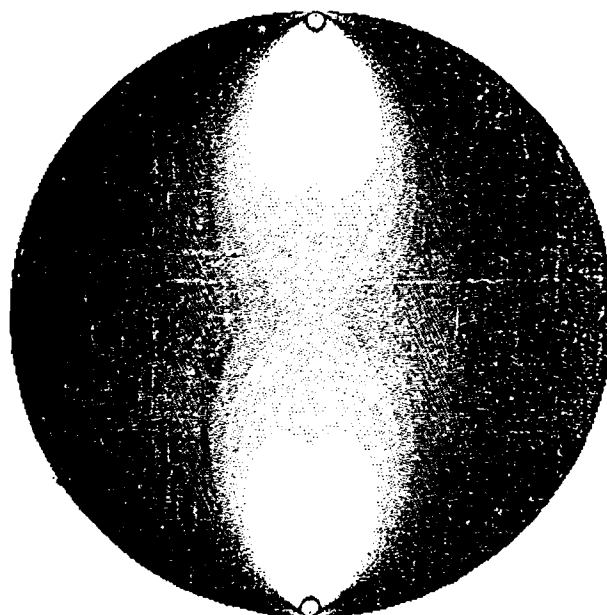
Fig. 3.2.2. a) Experimentally observed and b) computed images on a (111) silicon disc of radius 0.873 cm, thickness 0.16 cm for a load of 38 kg and the angle of polarization α of 90° . Normalized intensity is plotted on a logarithmic scale for the computed image.



(a)

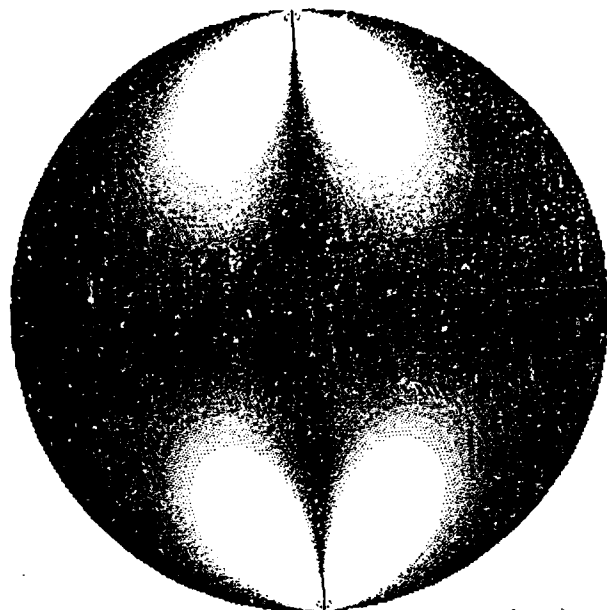


(b)



(c)

Fig. 3.2.3. a) Experimentally observed image reported by Appel et.al. [11] for a silicon sample of unknown orientation with a radius of 0.437 cm, thickness of 0.188 cm, load of 38 kg and the angle of polarization α of the incident light of 60° , b) simulated image for the same conditions as a) for (100) orientation, and c) same as b) but for (111) orientation. Normalized intensity is plotted on a logarithmic scale for the computed images.

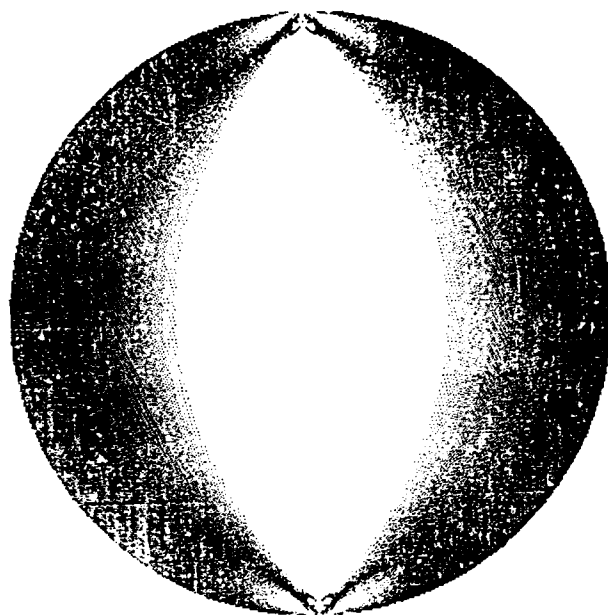


(a)



(b)

Fig. 3.2.4. a) Simulated image on a (100) gallium arsenide disc of radius 0.375 inch and thickness 65 mils. Diametrical compression load $P = 20$ kg, angle of polarization $\alpha = 0^\circ$. b) Experimentally obtained image for the same conditions as a). Normalized intensity is plotted on a logarithmic scale for the simulated image.



(a)



(b)

Fig. 3.2.5. a) Simulated image on a (100) gallium arsenide disc of radius 0.375 inch and thickness 65 mils. Diametrical compression load $P = 40$ kg, angle of polarization $\alpha = 45^\circ$. b) Experimentally obtained image for the same conditions as a). Normalized intensity is plotted on a logarithmic scale for the simulated image.

3.3 Stress-Optic Coefficient

Isotropic materials with spherical indicatrices become anisotropic when stressed either by some external means such as application of a load or by internal means such as defects within the material. The stress field causes optical anisotropy and as a result the material becomes birefringent with the indicatrix represented by an ellipsoid. Thus, if the sample is illuminated with a monochromatic radiation of wavelength longer than the absorption cut-off of the material, upon entering the stressed sample, the light will split into two components along the major and the minor axes of the cross-sectional ellipse of the indicatrix with different indices of refraction. These two components will build up a phase difference ϕ between them as they traverse the sample. This phase difference is given by

$$\phi = \frac{C(\sigma_1 - \sigma_2)2\pi d}{\lambda}, \quad (3.3.1)$$

where C is the stress-optic coefficient of the material, σ_1 , and σ_2 are the diagonalized elements of the stress matrix given by

$$\sigma_1 = \frac{\sigma_{11} + \sigma_{22}}{2} + \frac{1}{2} \left[(\sigma_{11} - \sigma_{22})^2 + 4\sigma_{12}^2 \right]^{1/2}, \quad (3.3.2)$$

and

$$\sigma_2 = \frac{\sigma_{11} + \sigma_{22}}{2} - \frac{1}{2} \left[(\sigma_{11} - \sigma_{22})^2 + 4\sigma_{12}^2 \right]^{1/2}, \quad (3.3.3)$$

where σ_{11} , σ_{22} , and σ_{12} are given by Eqns.(2.1.1-2.1.3) respectively, d is the material thickness, and λ is the wavelength of the incident light. This approach assumes a constant value of the stress-optic coefficient. However, the stress-optic coefficient can be taken as a constant only for isotropic materials. In an anisotropic medium, which is the case for a diametrically compressed semiconductor sample, the value of the stress-optic coefficient C will depend on the orientation of the load with respect to the principal crystal axes. The values of C will also vary, in general, from one point of the sample surface to the next for a given load. However, the values of C do not depend on the magnitude of the applied load, provided that a linear relationship between the pressure and the phase retardation holds. Giardini [2] has reported that this linearity holds upto a pressure of 450 kg/cm² for silicon.

In this work, a different approach is taken to examine the behavior of the stress-optic coefficient C for the case of diametrically compressed discs of semiconductors (silicon and gallium arsenide). The incident light while passing through the stressed sample splits into two components with different indices of refraction, and thus travels with different velocities. The velocity of light within a material with index of refraction n is given by c/n , where c is the velocity of light in free space. Now it is assumed that the light travelling along the minor axis of the ellipse has a velocity v_1 , and that travelling along the major axis has a velocity v_2 , with corresponding wavelengths λ_1 and λ_2 , and the indices of refraction n_1 and n_2 . The phase angle of the minor axis component is given by

$\phi_1 = 2\pi d/\lambda_1$, and that of the major axis component is given by $\phi_2 = 2\pi d/\lambda_2$. The phase angle difference ϕ between these two components is given by

$$\phi = \phi_2 - \phi_1 = 2\pi d \left(\frac{1}{\lambda_2} - \frac{1}{\lambda_1} \right),$$

or,

$$\phi = 2\pi d \left(\frac{n_2 f}{c} - \frac{n_1 f}{c} \right),$$

or,

$$\phi = \frac{2\pi d}{\lambda} (n_2 - n_1) \quad (3.3.4)$$

where λ is the wavelength of the incident light in free space and f is its frequency.

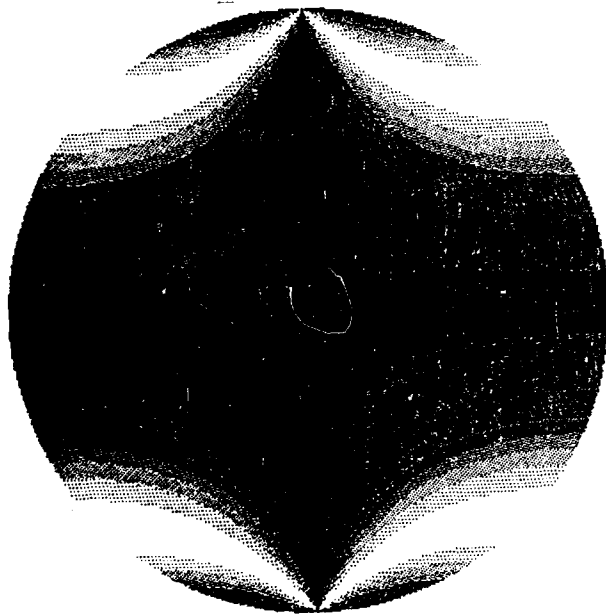
Comparison of Eqns.(3.3.1) and (3.3.4) gives

$$C = \frac{n_2 - n_1}{\sigma_1 - \sigma_2} \quad (3.3.5)$$

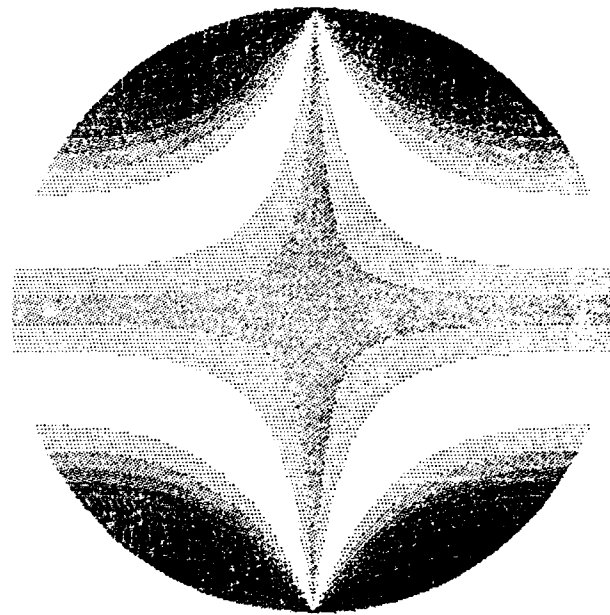
Equation (3.3.5) was used to compute the value of C at each point on the wafer for a semiconductor disc under diametrical compression. For both Si and GaAs (100) samples, the value of C was found to vary along the sample surfaces. The value of C was also found to depend on the orientation of the load with respect to the principal crystal axes. However, for both Si and GaAs (111) samples, C was found to be independent of the loading orientation or the position on the sample surfaces as expected from the crystal symmetry.

The values of C calculated from the simulation as a function of position on the sample surface for a (100) oriented silicon disc are shown in Fig.3.3.1. Figure 3.3.2 shows the same for a (100) oriented gallium arsenide disc. In both of these figures, the orientation of the load with respect to the principal crystal axes lying on the wafer surface is defined by the angle δ . Figure 3.3.1(a) shows the values of the stress-optic coefficient C as a function of position on a (100) Si surface for $\delta = 45^\circ$, while Fig.3.3.1(b) shows the same for $\delta = 75^\circ$. Similarly, Figs.3.3.2(a) and 3.3.2(b) show the values of C for a (100) GaAs sample for the angles $\delta = 45^\circ$, and $\delta = 75^\circ$, respectively.

From Figs.3.3.1 and 3.3.2 it can be seen clearly that, as expected, C cannot be taken as a constant for a given load as it is a function of position on the sample surface. As the angle of loading is changed, the pattern of C on the wafer changes. Therefore, it is a function of the orientation of the loading axes with respect to the principal crystal directions. For (100) oriented silicon, the values of C ranged from $2.0 \times 10^{-12} \text{ cm}^2/\text{dyne}$ to $3.0 \times 10^{-12} \text{ cm}^2/\text{dyne}$ and is plotted in Fig.3.3.1 in a gray scale with 11 levels. In the plot, a white scale was employed for $C > 2.95 \times 10^{-12} \text{ cm}^2/\text{dyne}$ and a black scale for $C < 2.05 \times 10^{-12} \text{ cm}^2/\text{dyne}$. Intermediate values were plotted in nine levels varying in the shade of gray, with linear spacings. For (100) oriented gallium arsenide, the values of C ranged from $0.8 \times 10^{-12} \text{ cm}^2/\text{dyne}$ to $2.6 \times 10^{-12} \text{ cm}^2/\text{dyne}$ and are plotted in Fig.3.3.2 in a gray scale with 10 levels. In the plot, a white scale was employed for

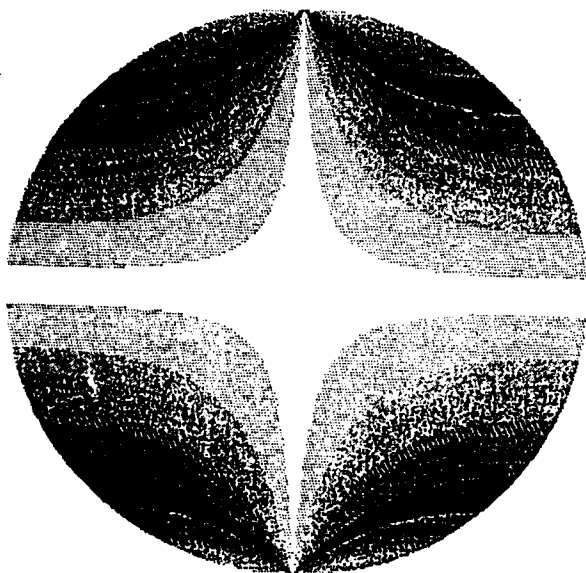


(a)

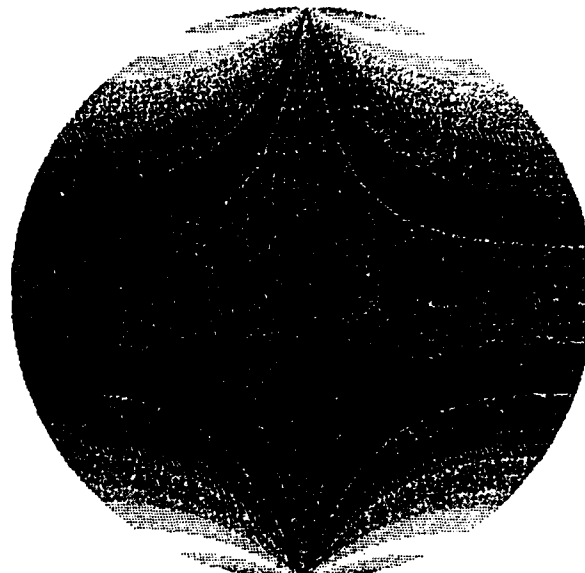


(b)

Fig. 3.3.1 Wafer map of the computed values of the stress-optic coefficient C for a) $\delta = 45^\circ$ and b) $\delta = 75^\circ$ for a load of 19 kg, (100) silicon wafer with radius of 0.873 cm and thickness of 0.16 cm. Plotted in 11 levels of gray scale with white for $C > 2.95 \times 10^{-12} \text{ cm}^2/\text{dyne}$ and black for $C < 2.05 \times 10^{-12} \text{ cm}^2/\text{dyne}$.



(a)



(b)

Fig. 3.3.2 Wafer map of the computed values of the stress-optic coefficient C for a) $\delta = 45^\circ$ and b) $\delta = 75^\circ$ for a load of 20 kg, (100) gallium arsenide wafer with radius of 0.375 inch and thickness of 65 mils. Plotted in 10 levels of gray scale with white for $C > 2.5 \times 10^{-12} \text{ cm}^2/\text{dyne}$ and black for $C < 0.9 \times 10^{-12} \text{ cm}^2/\text{dyne}$.

$C > 2.5 \times 10^{-12} \text{ cm}^2/\text{dyne}$ and a black scale for $C < 0.9 \times 10^{-12} \text{ cm}^2/\text{dyne}$. Intermediate values were plotted in eight levels varying in the shade of gray, with linear spacings.

One important point to note is that though C varies as a function of position for any given load, yet for a given value of δ , the wafer map of C is independent of the magnitude of the applied load. For instance, Fig.3.3.1 is plotted for a load of 19 kg and Fig.3.3.2 is plotted for a load of 20 kg. However, doubling the load to 38 and 40 kg respectively will not cause these two patterns to change. This is expected from the linearity between the stress and the phase retardation.

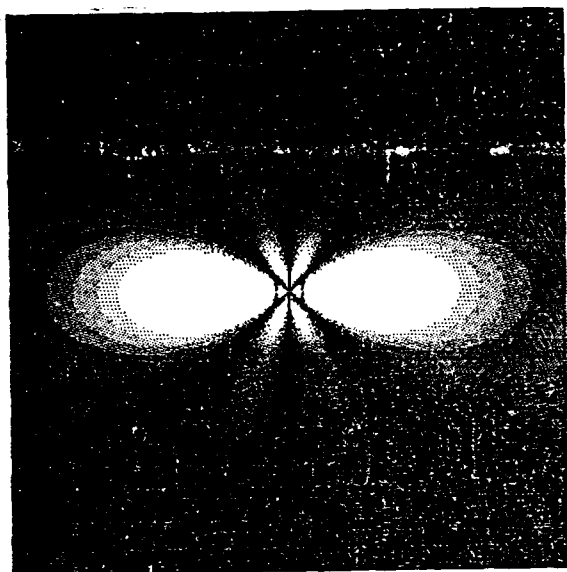
However, for (111) oriented Silicon or Gallium Arsenide, the value of C is independent of position for any given load, and is also independent of the orientation of the loading axes with respect to the principal crystal axes. The value we report for (111) silicon disc under diametrical compression is $2.33 \times 10^{-12} \text{ cm}^2/\text{dyne}$ and the same for Gallium Arsenide disc under diametrical compression is $1.94 \times 10^{-12} \text{ cm}^2/\text{dyne}$.

The value of C quoted by Appel et.al. [11] for silicon is $2.1 \times 10^{-12} \text{ cm}^2/\text{dyne}$. Bullough [12] reported it as variable from $1.0 \times 10^{-12} \text{ cm}^2/\text{dyne}$ to $2.3 \times 10^{-12} \text{ cm}^2/\text{dyne}$ based on his studies of edge dislocations in silicon. Prussin and Stevenson [13] deduced a value of $2.0 \times 10^{-12} \text{ cm}^2/\text{dyne}$ in their experiment on silicon bars subjected to pure bending. Their reported value compares favorably to those quoted by Bullough and by Appel et.al. Both the works by Appel et.al. and by Prussin and Stevenson measured the retardation as a function of the applied stress. From the observed linear relation between them, a mean value of the stress-optic coefficient C was found to fit the data, whereas Bullough adjusted the value of C to make his theoretical simulation of edge dislocations in silicon match with those experimentally determined by Bond and Andrus [14].

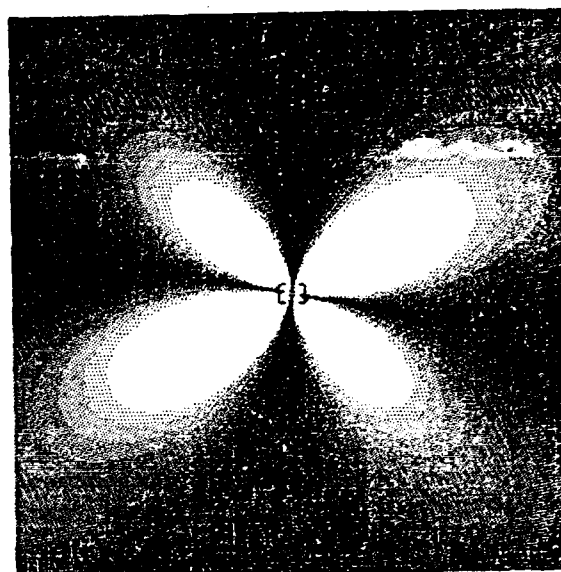
To summarize, we can say that for (100) oriented Silicon or Gallium Arsenide disc under diametrical compression, no unique value of C can be given as it varies from point to point for any given load, and varies with the orientation of the load with respect to the principal crystal axes as well. However, no such dependence was found for (111) oriented samples. For silicon, the values of C calculated in this work are consistent with those reported earlier. However for gallium arsenide to our knowledge, no data of C is reported so far. The value of C for a given position on the wafer will not change on increasing the load so long as the tensor elements π_{ijkl} of the piezo-optic coefficient matrix remain constant.

3.4 Simulation Results for Edge and Screw Dislocations

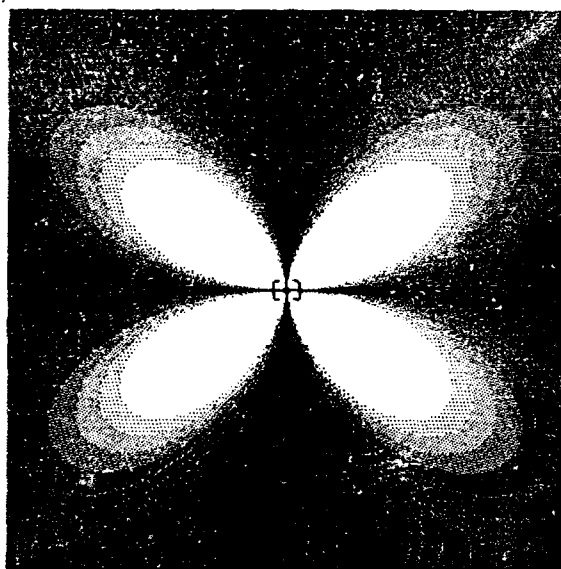
The simulation results for edge and screw dislocations are presented in this Subsection. Figure 3.4.1 shows the simulation results for an edge dislocation on a (100) Si surface with the dislocation slip plane lying on one of the principal crystal plane and the Burgers vector along one of the principal crystal direction (i.e., the angle ψ in Fig.2.2.1 is zero). The polarization angle of the incident light with respect to the dislocation slip plane is denoted by α . The images in Fig.3.4.1 are obtained for the light



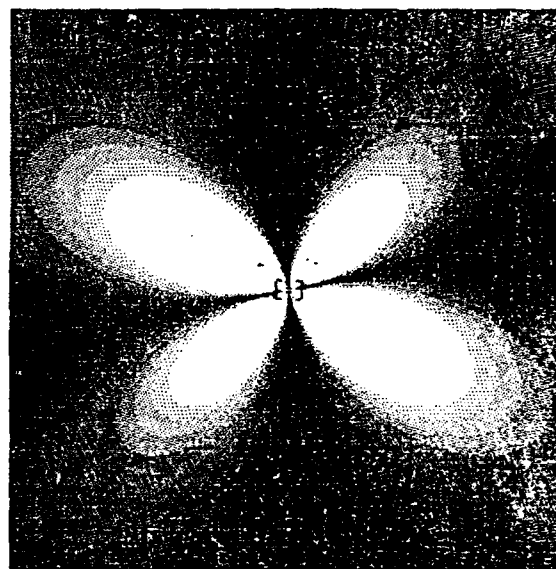
(a)



(b)



(c)



(d)

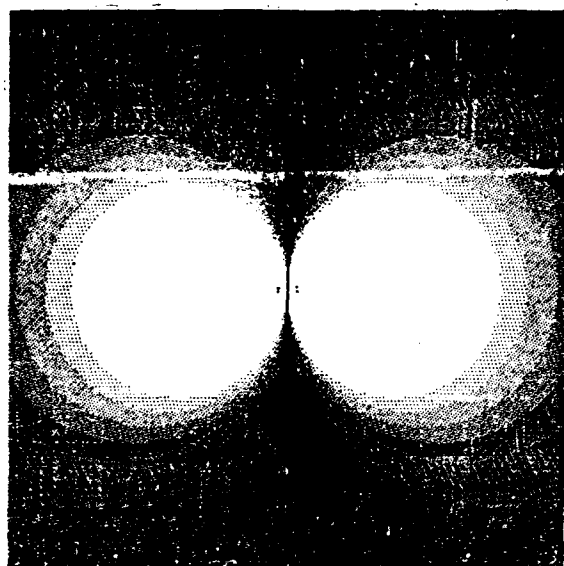
Fig. 3.4.1 Simulated fringe patterns for an edge dislocation on a (100) Si surface with the dislocation slip plane along one of the principal crystal plane and the Burger's vector along one of the principal crystal direction. α is the angle between the dislocation slip plane and the polarization axis of the incident light. a) $\alpha = 0^\circ$, b) $\alpha = 30^\circ$, c) $\alpha = 45^\circ$, d) $\alpha = 60^\circ$.

incident along one of the principal crystal direction. Figures 3.4.1(a), (b), (c), and (d) show the simulation results for $\alpha = 0^\circ$, 30° , 45° , and 60° , respectively. From the figures, it can clearly be seen that when the polarizer makes an angle of 45° with respect to the dislocation slip plane, the image is brightest with a four-petal rosette pattern with equal lobes. This is of interest as it is a key feature which distinguishes edge dislocations from screw dislocations lying along principal crystal planes, as will be evident from the following paragraphs.

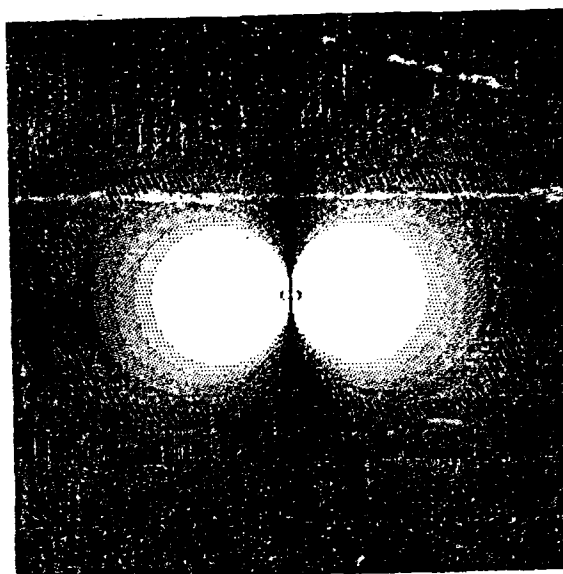
Figure 3.4.2 shows the simulation results for a screw dislocation on a (100) Si surface with the dislocation slip plane lying along one of the principal crystal plane and the Burgers vector along one of the principal crystal direction. Here also the polarization angle of the incident light with respect to the dislocation slip plane is denoted by α . If the light is incident along the direction of the Burgers vector, the cross-section is a circle and there is no birefringence as is evident from Eqn.(2.3.16). Therefore, for the particular case under consideration, this dislocation cannot be viewed end-on, i.e., along the direction of the Burgers vector. Figures 3.4.2(a), (b), (c), and (d) show the simulation results for a screw dislocation when the light is incident perpendicular to the direction of the Burgers vector and along one of the principal crystal direction for $\alpha = 0^\circ$, 25° , 50° , and 75° , respectively. From the intensity distribution equation (2.3.19) for a screw dislocation, we can see that for $\alpha = \beta = 45^\circ$, there is a total extinction as the transmitted intensity is zero. However, for edge dislocations for $\alpha = 45^\circ$, the intensity distribution is brightest with a four-petal rosette pattern with equal lobes.

Therefore, for these two specific cases under investigation, it is easy to find out the types of the dislocations, their locations, and their orientations by continuously varying the polarization angle and monitoring the fringe patterns closely. The orientation of a screw dislocation is 45° from the axis of polarization for total extinction. For any other angles of polarization, the images of edge and screw dislocations are completely different as evident upon comparing Figs.3.4.1 and 3.4.2. However, these figures are obtained under rather restrictive assumptions of the orientations of the dislocations and the incident light directions.

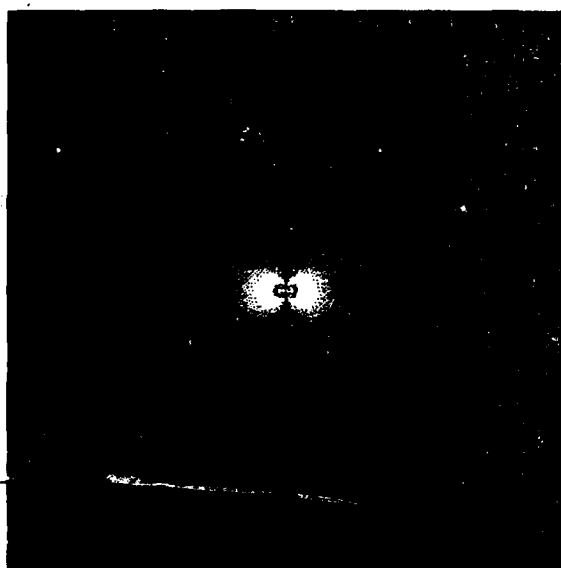
This simulation approach can be made quite general though it would be rather tedious to work out for any arbitrary orientation of the dislocation slip plane with respect to any of the principal crystal planes, and any arbitrary direction of the Burgers vector with respect to the dislocation slip plane. The approach would include determining the direction cosines between the dislocation slip plane and the principal crystal directions. Then any arbitrary orientation of the Burgers vector with respect to the dislocation slip plane can be taken care of by resolving it along the dislocation slip plane and perpendicular to it which would then give the edge and the screw components. Then the stress components form each of these two types of defects need to be added keeping in perspective the directions of the principal stress components and the shear stress components. Then these added stress components need to be transformed to the principal crystal directions from the known values of the direction cosines between the principal crystal directions and the dislocation slip plane. After that, the changes in the dielectric impermeability can be obtained from the known values of the piezo-optic coefficients.



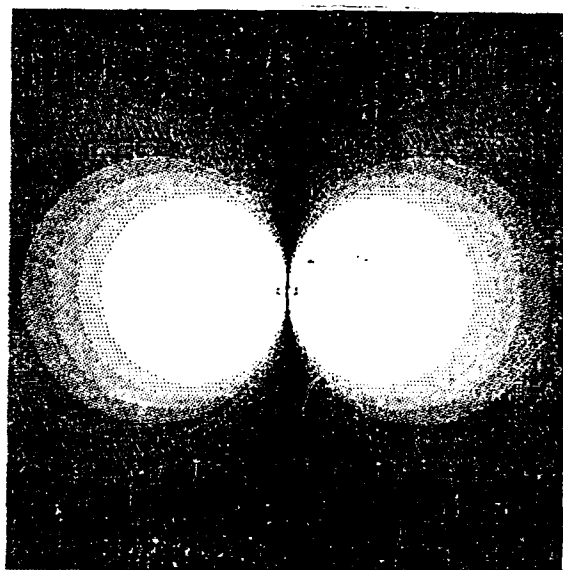
(a)



(b)



(c)



(d)

Fig.3.4.2 Simulated fringe patterns for a screw dislocation on a (100) Si surface with the dislocation slip plane along one of the principal crystal plane and the Burger's vector along one of the principal crystal direction. α is the angle between the dislocation slip plane and the polarization axis of the incident light a) $\alpha = 0^\circ$, b) $\alpha = 25^\circ$, c) $\alpha = 50^\circ$, d) $\alpha = 75^\circ$.

Then we need to fix the direction of the incident light with respect to these principal crystal directions and obtain the direction cosines between them. After that the changes in the dielectric impermeability obtained in the principal crystal axes need to be transformed to the coordinate system determined by the light direction from the known values of the direction cosines. The diagonalization of the dielectric impermeability matrix then follows to obtain the refractive indices along the major and the minor axes directions and then the procedure of obtaining the intensity of the light transmitted through the analyzer is the same as outlined in either of the Sections 2.2, or 2.3.

Thus, the generalization of the problem is straightforward in concept but the algebra involved is sufficiently complicated. Currently work is being done to make this algorithm more general in approach. A variety of these images for varying directions of the Burgers vector with respect to the dislocation slip plane and varying orientations of the dislocation slip plane with respect to the principal crystal planes for varying directions of the incident light and varying angles of polarization can be generated and stored on the computer. Then a sample with any arbitrary direction of the Burgers vector and any arbitrary orientation of the dislocation slip plane can be placed under the polariscope and the experimental image obtained for different directions of the incident light and different angles of polarization. Then an image matching procedure is needed between the simulated images and the experimentally observed ones to determine the exact direction of the Burgers vector and the exact orientation of the dislocation slip plane.

4. SUMMARY AND CONCLUSIONS

A fast, accurate, and efficient technique which can characterize large defects in each semiconductor substrate prior to device fabrication in a reasonable time will improve the yield of the electronic devices fabricated on it. In this work, the technique of infrared piezo-birefringence is investigated to characterize large defects in semiconductor materials. A dark field plane polariscope using $1.15\text{ }\mu\text{m}$ wavelength He-Ne infrared laser as the light source was constructed for this purpose.

As a first step towards defect characterization, the cases of diametrically loaded discs of semiconductor samples were taken. An algorithm was developed to be used in the computer for the simulation of the stress patterns and the resulting fringe patterns for infrared transparent semiconductor discs under diametrical compression placed in a dark field plane polariscope between crossed polarizer and analyzer. This was done to obtain a better understanding of the simulation algorithm and subsequently for its use for defect characterization. The simulation results matched remarkably well with the experimentally obtained images for diametrically compressed discs of Si and GaAs.

The behavior of the stress-optic coefficient C was also investigated in this work, which had been taken as a constant in earlier works by other investigators. Our investigation showed that for (100) oriented Si and GaAs discs under diametrical compression, the value of C changed from one point to the next on the sample surface for a given load. The value of C was also found to depend on the orientation of the applied load with respect to the principal crystal axis. However, the value of C on any position on the wafer did not change upon increasing the magnitude of the load. This is expected from the linearity between the stress and the phase retardation. The values of C for both Si and GaAs discs of (111) orientation were found to be independent of position for any given load, as well as were independent of the orientation of the load with respect to the principal crystal axis, as expected from the crystal symmetry. The values we report for (100) Si disc subjected to diametrical compression ranged from $2.0 \times 10^{-12}\text{ cm}^2/\text{dyne}$ to $3.0 \times 10^{-12}\text{ cm}^2/\text{dyne}$, and for (100) GaAs disc subjected to diametrical compression ranged from $0.8 \times 10^{-12}\text{ cm}^2/\text{dyne}$ to $2.6 \times 10^{-12}\text{ cm}^2/\text{dyne}$. For (111) oriented Si and GaAs discs under diametrical compression, the values are $2.33 \times 10^{-12}\text{ cm}^2/\text{dyne}$ and $1.94 \times 10^{-12}\text{ cm}^2/\text{dyne}$, respectively.

Next the algorithm was used to determine the fringe patterns for edge and screw dislocations. For simplification purposes, image simulations were carried out for edge and screw dislocations when the dislocation line, the Burgers vector and the direction of the incident light were along the crystal principal axes. For this special case when the incident light was perpendicular to the Burgers vector, the image patterns for an edge and a screw dislocation were obtained and they showed a distinguishing difference between them. For the polarization angle of the light of 45° with respect to the dislocation slip plane, the image of a screw dislocation was found to disappear, whereas for an edge dislocation for the same polarization angle, the image pattern was the brightest with a four-petal rosette pattern with equal lobes. This feature was striking as it gave a distinguishing factor for detecting a screw dislocation from an edge dislocation by continuously varying the polarization angle and monitoring the fringe patterns.

Though specific cases were investigated here for the edge and the screw dislocations, the approach can be made quite general to take into account any arbitrary direction of the Burgers vector, the dislocation slip plane, the direction of the incident light, and the polarization angle of the incident light. The concept is rather straightforward but the algebra involved is sufficiently complicated and tedious. The general approach is given below.

First, the direction cosines between the dislocation slip plane and the principal crystal directions are obtained. Then any arbitrary direction of the Burgers vector with respect to the dislocation slip plane is taken into account by resolving it along the dislocation line and perpendicular to it, which are the screw and the edge components. Then the stress components for these two cases are added keeping in mind the actual stress directions of the principal stress components and the shear stress components. After that the added stress components are transformed to the crystal principal directions from the known values of the direction cosines between the principal crystal directions and the dislocation slip plane.

Then the changes in the dielectric impermeability along the principal crystal directions are obtained from the known values of the piezo-optic coefficients and the stress components. Then the direction of the incident light needs to be fixed with respect to the principal crystal directions and obtain the direction cosines between them. After that, the changes in the dielectric impermeability is transformed to the coordinate system defined by the light direction from the known values of the direction cosines. Then the diagonalization of the dielectric impermeability matrix follows to obtain the refractive indices along the major and the minor axes directions. After that, the usual procedure of obtaining the intensity of the transmitted light through the analyzer as outlined in Sections 2.2, or 2.3, can be utilized.

Currently work is being done to generate the images of edge and screw dislocations for varying directions of the Burgers vector, the dislocation slip plane, the incident light direction, and the polarization angle of the incident light. The simulation results can then be stored in a computer. Then a sample with any arbitrary direction of the Burgers vector and any arbitrary orientation of the dislocation slip plane can be placed under the polariscope and the experimental images obtained for varying directions and angles of polarization of the incident light. Then an image matching procedure can be utilized between the simulated images and the experimentally observed ones to determine the exact direction of the Burgers vector and the exact orientation of the dislocation slip plane.

5. REFERENCES

1. B.K.Tanner; X-Ray Diffraction Topography; Pergamon Press, 1976.
2. A.A.Giardini; "Piezobirefringence in Silicon"; The American Mineralogist; Vol. 43, p. 249, 1958.
3. S.R. Lederhandler; "Infrared Studies of Birefringence in Silicon"; Journal of Applied Physics; Vol. 30, p. 1631, 1959.
4. J. Hornstra and P. Penning; "Birefringence Due to Residual Stress in Silicon"; Philips Research Reports; Vol. 14, p. 237, 1959.
5. D.A. Jenkins and J.J. Hren; "Quantitative Piezobirefringence Studies of Dislocations in Transparent Crystals"; Philosophical Magazine; Vol. 33, p. 173, 1976.
6. D.A. Jenkins, T.S. Plaskett, and P. Chaudhuri; Birefringence Images of Arbitrarily Oriented Dislocation Lines in (111) Silicon Wafers"; Philosophical Magazine; Vol. 39, p. 237, 1979.
7. M.M. Frocht; Photoelasticity; John Wiley & Sons, 1941.
8. J.F. Nye; Physical Properties of Crystals; Clarendon Press, 1986.
9. H. Booyens and J.H. Basson; "The Application of Elastobirefringence to the Study of Strain Fields and Dislocations in III-V Compounds"; Journal of Applied Physics; Vol. 51, p. 4375, 1980.
10. J.P. Hirth and J. Lothe; "Theory of Dislocations"; McGraw-Hill, 1968.
11. A.V. Appel, H.T. Betz, and D.A. Pontarelli; "Infrared Polariscopes for Photoelastic Measurement of Semiconductors"; Applied Optics; Vol. 4, p. 1475, 1965.
12. R. Bullough; "Birefringence Caused by Edge Dislocations in Silicon"; Physical Review; Vol. 110, p. 620, 1958.
13. S. Prussin and A. Stevenson; "Strain-Optic Coefficient of Silicon for Infrared Light"; Journal of Applied Physics; Vol. 30, p. 452, 1959.
14. W.L. Bond and J. Andrus; "Photographs of the Stress Field Around Edge Dislocations"; Physical Review; Vol. 101, p. 1211, 1956.

6. APPENDICES

6.1 Direction Cosines for a (100) Plane under Arbitrary Loading

Figure 6.1.1 shows the axes system chosen. The loading axes system is (x_1, x_2, x_3) and the crystal principal axes system is (x'_1, x'_2, x'_3) . Axis x_3 in the loading axes system and axis x'_1 in the crystal principal axes system come out of the plane of the paper. The crystal principal axis x'_2 makes an angle α with axis x_1 of the loading axes system. The load P is applied along axis x_2 . The coordinates being so defined, the direction cosines can now be obtained. These are given by

$$\begin{aligned}a_{11} &= \cos x'_1 \wedge x_1 = \cos 90 = 0, \\a_{12} &= \cos x'_1 \wedge x_2 = \cos 90 = 0, \\a_{13} &= \cos x'_1 \wedge x_3 = \cos 0 = 1, \\a_{21} &= \cos x'_2 \wedge x_1 = \cos \alpha, \\a_{22} &= \cos x'_2 \wedge x_2 = \cos (90 - \alpha), \\a_{23} &= \cos x'_2 \wedge x_3 = \cos 90 = 0, \\a_{31} &= \cos x'_3 \wedge x_1 = \cos (90 + \alpha), \\a_{32} &= \cos x'_3 \wedge x_2 = \cos \alpha, \\a_{33} &= \cos x'_3 \wedge x_3 = \cos 90 = 0.\end{aligned}\tag{6.1.1}$$

6.2 Direction Cosines for a (111) Plane under Arbitrary Loading

The case for (111) plane is more involved. Here, (x_1, x_2, x_3) coordinate system refers to the loading axes system with x_2 being the axis of loading. Axis x_1 lies on the sample surface while axis x_3 is normal to the plane of the paper as shown in Fig. 6.2.1. Also, (x'_1, x'_2, x'_3) refers to the crystal principal axes coordinate system as shown in Fig. 6.2.2. The origin of both these coordinate systems is taken to be the substrate center 0.

Let (x_1, x_2, x_3) be the point on the wafer periphery where the load is applied. This arbitrary loading direction can be specified by an angle γ measured in the clockwise direction from axis x''_2 as shown in Fig. 6.2.3(a). The latter is the projection of crystal principal axis x'_1 on the wafer plane as indicated in Fig. 6.2.3(b). Axes x_3 and x''_3 are the same axis normal to the plane of the paper. Axis x''_1 is in the plane of the wafer and is perpendicular to both x''_2 and x''_3 . We need to determine the direction cosines a_{ij} that relate a point (x_1, x_2, x_3) in the loading

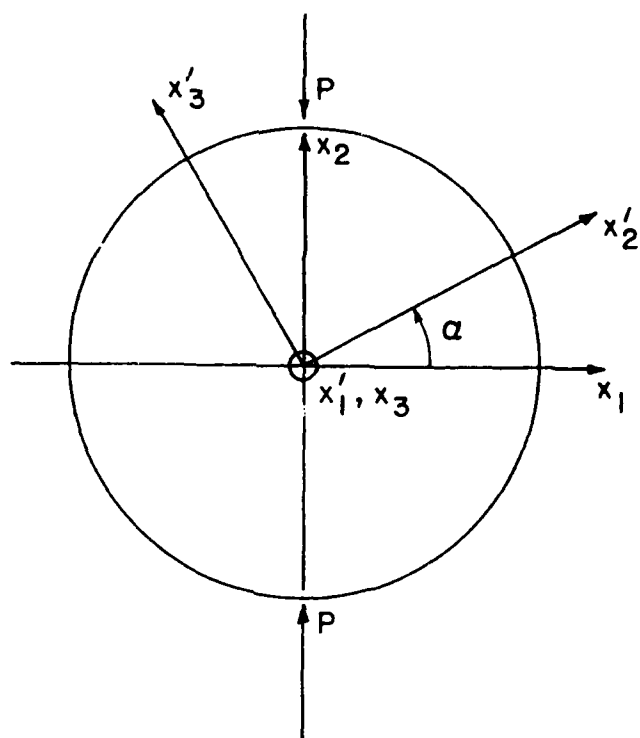


Fig.6.1.1 The loading and the crystal principal axes systems for a (100) plane.

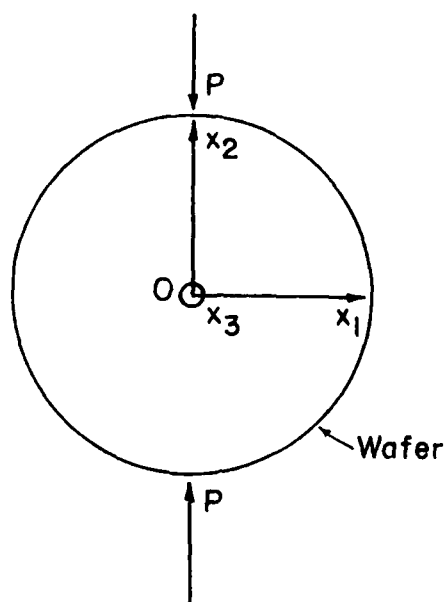


Fig.6.2.1 The loading axes coordinate system.

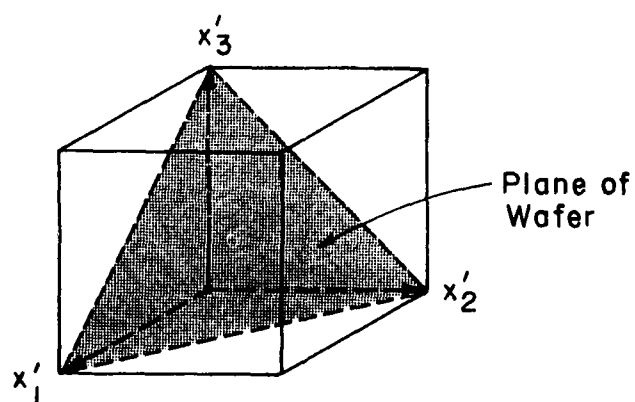
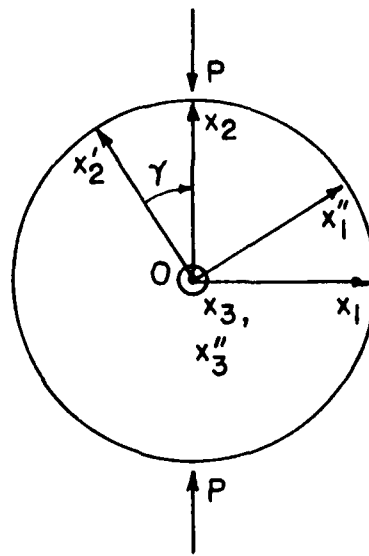
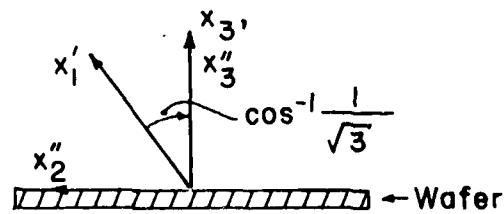


Fig.6.2.2 The crystal axes system and its orientation with respect to the plane of the wafer.



(a) Top view



(b) Side view

Fig.6.2.3 The (x''_1, x''_2, x''_3) coordinate system and its relationship to the loading axes system and the crystal principal axes system.

axes system to a point (x_1', x_2', x_3') in the crystal axes system. The transformation equation is given as

$$x_i' = \sum_j a_{ij} x_j \quad (j=1,2,3). \quad (6.2.1)$$

This linear transformation is carried out in two steps as given below

$$x_k'' = \sum_j a_{kj}'' x_j \quad (j=1,2,3),$$

and
$$x_i' = \sum_k a_{ik}'' x_k'' \quad (k=1,2,3),$$

or
$$x_i' = \sum_k a_{ik}'' \left(\sum_j a_{kj}'' x_j \right). \quad (6.2.2)$$

Comparing Eqns.(6.2.1) and (6.2.2) gives

and
$$a_{ij} = \sum_k a_{ik}'' a_{kj}' \quad (k=1,2,3). \quad (6.2.3)$$

From Fig.6.2.3, one obtains by direct observation that

$$\begin{aligned} a_{11}' &= \cos(x_1'' \wedge x_1) = \cos \gamma, \\ a_{12}' &= \cos(x_1'' \wedge x_2) = \cos(90^\circ - \gamma), \\ a_{13}' &= \cos(x_1'' \wedge x_3) = 0, \\ a_{21}' &= \cos(x_2'' \wedge x_1) = \cos(90^\circ + \gamma), \\ a_{22}' &= \cos(x_2'' \wedge x_2) = \cos \gamma, \\ a_{23}' &= \cos(x_2'' \wedge x_3) = 0, \\ a_{31}' &= \cos(x_3'' \wedge x_1) = 0, \\ a_{32}' &= \cos(x_3'' \wedge x_2) = 0, \\ a_{33}' &= \cos(x_3'' \wedge x_3) = 1. \end{aligned} \quad (6.2.4)$$

In the crystal axes system, from Fig.6.2.2, we can write the unit vector \hat{x}_2'' along the axis x_2''

$$\hat{x}_2'' = \frac{2}{\sqrt{6}} \hat{x}_1' - \frac{1}{\sqrt{6}} \hat{x}_2' - \frac{1}{\sqrt{6}} \hat{x}_3', \quad (6.2.5)$$

where \hat{x}_1' , \hat{x}_2' , \hat{x}_3' are unit vectors along the three crystal principal axes. This is obtained by considering the intercept of the (111) crystal plane on x_1' axis as $(a, 0, 0)$ and then by translating the origin by $(\frac{a}{3}, \frac{a}{3}, \frac{a}{3})$ to the substrate center to give the point coordinates as $(\frac{2a}{3}, -\frac{a}{3}, -\frac{a}{3})$. Here, a is the crystal lattice constant. The unit vector pointing from the origin $(0, 0, 0)$ to this point is given by Eqn.(6.2.5). The unit vector \hat{x}_3'' along the direction perpendicular to the (111) plane is given from analytical geometry as

$$\hat{x}_3'' = \frac{1}{\sqrt{3}} \hat{x}_1' + \frac{1}{\sqrt{3}} \hat{x}_2' + \frac{1}{\sqrt{3}} \hat{x}_3' . \quad (6.2.6)$$

The unit vector $\hat{x}_1'' = \hat{x}_2'' \times \hat{x}_3''$ and is given by

$$\hat{x}_1'' = -\frac{1}{\sqrt{2}} \hat{x}_2' + \frac{1}{\sqrt{2}} \hat{x}_3' . \quad (6.2.7)$$

Using Eqns.(6.2.5-6.2.7) gives

$$\begin{aligned} a_{11}'' &= \cos(\hat{x}_1' \hat{x}_1'') = 0, \\ a_{12}'' &= \cos(\hat{x}_1' \hat{x}_2'') = \cos(35.264^\circ) = 1/\sqrt{6}, \\ a_{13}'' &= \cos(\hat{x}_1' \hat{x}_3'') = \cos(54.736^\circ) = 1/\sqrt{3}, \\ a_{21}'' &= \cos(\hat{x}_2' \hat{x}_1'') = \cos(135^\circ) = -1/\sqrt{2}, \\ a_{22}'' &= \cos(\hat{x}_2' \hat{x}_2'') = \cos(114.095^\circ) = -1/\sqrt{6}, \\ a_{23}'' &= \cos(\hat{x}_2' \hat{x}_3'') = \cos(54.736^\circ) = 1/\sqrt{3}, \\ a_{31}'' &= \cos(\hat{x}_3' \hat{x}_1'') = \cos(45^\circ) = 1/\sqrt{2}, \\ a_{32}'' &= \cos(\hat{x}_3' \hat{x}_2'') = \cos(114.095^\circ) = -1/\sqrt{6}, \\ a_{33}'' &= \cos(\hat{x}_3' \hat{x}_3'') = \cos(54.736^\circ) = 1/\sqrt{3}. \end{aligned} \quad (6.2.8)$$

Using Eqns.(6.2.4) and (6.2.8), we can get the direction cosines a_{ij} from Eqn.(6.2.3). These are given by

$$\begin{aligned}
 a_{11} &= \frac{2}{\sqrt{6}} \cos(90^\circ + \gamma), \\
 a_{12} &= \frac{2}{\sqrt{6}} \cos \gamma, \\
 a_{13} &= \frac{1}{\sqrt{3}}, \\
 a_{21} &= -\frac{1}{\sqrt{2}} \cos \gamma - \frac{1}{\sqrt{6}} \cos(90^\circ + \gamma), \\
 a_{22} &= -\frac{1}{\sqrt{2}} \cos(90^\circ - \gamma) - \frac{1}{\sqrt{6}} \cos \gamma, \\
 a_{23} &= \frac{1}{\sqrt{3}}, \\
 a_{31} &= \frac{1}{\sqrt{2}} \cos \gamma - \frac{1}{\sqrt{6}} \cos(90^\circ + \gamma), \\
 a_{32} &= \frac{1}{\sqrt{2}} \cos(90^\circ - \gamma) - \frac{1}{\sqrt{6}} \cos \gamma, \\
 a_{33} &= \frac{1}{\sqrt{3}}.
 \end{aligned} \tag{6.2.9}$$

For the special case when the loading axis x_2 coincides with the axis x_2'' , $\gamma = 0$ and

$$\begin{aligned}
 a_{11} &= 0, \quad a_{12} = \frac{2}{\sqrt{6}}, \quad a_{13} = \frac{1}{\sqrt{3}}, \quad a_{21} = -\frac{1}{\sqrt{2}}, \quad a_{22} = -\frac{1}{\sqrt{6}}, \\
 a_{23} &= \frac{1}{\sqrt{3}}, \quad a_{31} = \frac{1}{\sqrt{2}}, \quad a_{32} = -\frac{1}{\sqrt{6}}, \quad \text{and} \quad a_{33} = \frac{1}{\sqrt{3}}.
 \end{aligned}$$

For any other value of γ , the direction cosines are given by Eqn.(6.2.9).

6.3 Piezo-Optic Coefficients for Gallium Arsenide from the Elasto-Optic and the Stiffness Coefficients

In this section, the piezo-optic coefficients for GaAs are derived from the elasto-optic and the stiffness coefficients. The notations used by Nye [8] are followed. The compliance is denoted by s , the stiffness by c , the elasto-optic coefficients by p , and the piezo-optic coefficients by π .

All of these parameters are fourth-rank tensors with each of them having a total of possible 81 terms. The generalized form of Hooke's law can be written as:

$$\epsilon_{ij} = \sum_{k,l} s_{ijkl} \sigma_{kl} \quad (k=1,2,3; \quad l=1,2,3), \quad (6.3.1)$$

where k and l are summation indices, the ϵ_{ij} denotes strain, the σ_{kl} denotes stress, and the s_{ijkl} denotes crystal compliance. Equation (6.3.1) can also be written in an alternate form as

$$\sigma_{ij} = \sum_{k,l} c_{ijkl} \epsilon_{kl} \quad (k=1,2,3; \quad l=1,2,3), \quad (6.3.2)$$

where c_{ijkl} are the stiffness constants of the crystal. For both s_{ijkl} and c_{ijkl} , the following relations are true

$$s_{ijkl} = s_{ijlk} = s_{jikl} = s_{jilk},$$

and

$$c_{ijkl} = c_{ijlk} = c_{jikl} = c_{jilk}. \quad (6.3.3)$$

Using the reduced notation of Nye as given in Table 2.1.1, Eqns.(6.3.1) and (6.3.2) can be written as

$$\epsilon_i = \sum_j s_{ij} \sigma_j \quad (i,j=1,2,\dots,6),$$

and

$$\sigma_i = \sum_j c_{ij} \epsilon_j \quad (i,j=1,2,\dots,6). \quad (6.3.4)$$

However, changing the notation from tensor to matrix introduces factors of 2 and 4 as follows. For the compliances:

$$s_{ijkl} = s_{mn} \text{ when } m \text{ and } n \text{ are } 1, 2 \text{ or } 3,$$

$$2s_{ijkl} = s_{mn} \text{ when either } m \text{ or } n \text{ are } 4, 5 \text{ or } 6,$$

$$4s_{ijkl} = s_{mn} \text{ when both } m \text{ and } n \text{ are } 4, 5 \text{ or } 6. \quad (6.3.5)$$

However, for the stiffness no factors of 2 or 4 are necessary. It can simply be written as:

$$c_{ijkl} = c_{mn} \quad (i,j,k,l=1,2,3; \quad m,n=1,2,\dots,6). \quad (6.3.6)$$

The total maximum possible number of non-equal elements after taking into account the identities (6.3.3) is 36. However, as the crystal possesses more

and more symmetry elements, the number of non-equal parameters reduces. For the cubic crystals, this number becomes only three with the matrix elements given by

$$\begin{bmatrix} x_{11} & x_{12} & x_{12} & 0 & 0 & 0 \\ x_{12} & x_{11} & x_{12} & 0 & 0 & 0 \\ x_{12} & x_{12} & x_{11} & 0 & 0 & 0 \\ 0 & 0 & 0 & x_{44} & 0 & 0 \\ 0 & 0 & 0 & 0 & x_{44} & 0 \\ 0 & 0 & 0 & 0 & 0 & x_{44} \end{bmatrix} \quad (6.3.7)$$

where x can stand for c , s , p , or π .

For cubic systems, s_{11} , s_{12} , s_{44} and c_{11} , c_{12} , c_{44} , are related by [8]

$$\frac{s_{11} + s_{12}}{(s_{11} - s_{12})(s_{11} + 2s_{12})} = c_{11},$$

$$\frac{-s_{12}}{(s_{11} - s_{12})(s_{11} + 2s_{12})} = c_{12},$$

and
$$s_{44} = \frac{1}{c_{44}}. \quad (6.3.8)$$

Solving the above equations for s_{11} and s_{12} , we get:

$$s_{11} = \frac{c_{11} + c_{12}}{(c_{11} - c_{12})(c_{11} + 2c_{12})},$$

$$s_{12} = \frac{-c_{12}}{(c_{11} - c_{12})(c_{11} + 2c_{12})}. \quad (6.3.9)$$

In the absence of any applied electric field, the change in the dielectric impermeability due to the strain can be given as [8]

$$\Delta B_{ij} = \sum_{r,s} p_{ijrs} \epsilon_{rs} \quad (r=1,2,3; s=1,2,3), \quad (6.3.10)$$

where

$$p_{ijrs} = \sum_{k,l} \pi_{ijk l} c_{klrs} \quad (k=1,2,3; l=1,2,3), \quad (6.3.11)$$

and

$$\pi_{ijk l} = \sum_{r,s} p_{ijrs} s_{rsk l} \quad (r=1,2,3; s=1,2,3). \quad (6.3.12)$$

The elasto-optic coefficients p_{ijrs} are dimensionless, whereas the piezo-optic coefficients π_{ijkl} have the dimension of stress. Both π and p follow the same matrix form in reduced notation as given in Eqn.(6.3.7).

Equation (6.3.12) can be written in the reduced form as:

$$\pi_{mn} = \sum_r p_{mr} s_{rn} \quad (r=1,2,\dots,6), \quad (6.3.13)$$

where m and n can take on values between 1 and 6. However, for cubic systems, as is the case here, the only possible values of non-zero and non-equal components are π_{11} , π_{12} , and π_{44} . The non-zero components are defined by the identities

- 1) $\pi_{11} = \pi_{22} = \pi_{33}$,
- 2) $\pi_{12} = \pi_{23} = \pi_{31} = \pi_{13} = \pi_{32} = \pi_{21}$,
- 3) $\pi_{44} = \pi_{55} = \pi_{66}$.

The rest of the components are zero.

From Eqn.(6.3.13)

$$\begin{aligned} \pi_{11} &= \sum_r p_{1r} s_{r1} \quad (r=1,2,\dots,6) \\ &= p_{11}s_{11} + p_{12}s_{21} + p_{13}s_{31} + p_{14}s_{41} + p_{15}s_{51} + p_{16}s_{61}. \end{aligned}$$

Now, $s_{21} = s_{31} = s_{12}$, $p_{13} = p_{12}$, and $p_{14} = p_{15} = p_{16} = 0$. Therefore,

$$\pi_{11} = p_{11}s_{11} + 2p_{12}s_{12}. \quad (6.3.14)$$

Similarly,

$$\begin{aligned} \pi_{12} &= \sum_r p_{1r} s_{r2} \quad (r=1,2,\dots,6) \\ &= p_{11}s_{12} + p_{12}s_{22} + p_{13}s_{32} + p_{14}s_{42} + p_{15}s_{52} + p_{16}s_{62}. \end{aligned}$$

Remembering the above relations and also $s_{22} = s_{11}$, the above equation reduces to

$$\pi_{12} = p_{11}s_{12} + p_{12}(s_{11} + s_{12}). \quad (6.3.15)$$

Also,

$$\begin{aligned} \pi_{44} &= \sum_r p_{4r} s_{r4} \quad (r=1,2,\dots,6) \\ &= p_{41}s_{14} + p_{42}s_{24} + p_{43}s_{34} + p_{44}s_{44} + p_{45}s_{54} + p_{46}s_{64} \end{aligned}$$

which reduces to

$$\pi_{44} = p_{44} s_{44}. \quad (6.3.16)$$

The values of p_{11} , p_{12} , and p_{44} , as well as of c_{11} , c_{12} , and c_{44} are given in the paper by Booyens and Basson [9] and are shown in Table 6.3.1.

Table 6.3.1

The values of the elasto-optic coefficients (p_{ij}) and the stiffness (c_{ij}) for GaAs after Booyens and Basson [9]
(p_{ij} are dimensionless, c_{ij} are in dyne/cm²)

p_{11}	p_{12}	p_{44}	c_{11}	c_{12}	c_{44}
-0.165	-0.14	-0.072	118.8×10^{10}	53.8×10^{10}	59.4×10^{10}

The coefficients c_{ij} are easily converted to the s_{ij} by Eqns.(6.3.8) and (6.3.9). This yields $s_{11} = 1.1728 \times 10^{-12}$ cm²/dyne, $s_{12} = -3.6558 \times 10^{-12}$ cm²/dyne, and $s_{44} = 1.6835 \times 10^{-12}$ cm²/dyne. Substituting for the values of s_{ij} obtained above and the values of p_{ij} from Table 6.3.1 in Eqns.(6.3.14-6.3.16), one obtains the piezo-optic coefficients as follows:

$$\pi_{11} = - 9.115 \times 10^{-14} \text{ cm}^2/\text{dyne},$$

$$\pi_{12} = - 5.269 \times 10^{-14} \text{ cm}^2/\text{dyne},$$

$$\text{and } \pi_{44} = - 1.212 \times 10^{-13} \text{ cm}^2/\text{dyne}. \quad (6.3.17)$$

However, for the π_{ij} , the following identities hold

$$\pi_{mn} = \pi_{ijkl} \quad \text{when } n=1,2,3,$$

and

$$\pi_{mn} = 2\pi_{ijkl} \quad \text{when } n=4,5,6.$$

Taking into account the above identities, the piezo-optic coefficients for GaAs are given as

$$\pi_{1111} = - 9.115 \times 10^{-14} \text{ cm}^2/\text{dyne},$$

$$\pi_{1122} = - 5.269 \times 10^{-14} \text{ cm}^2/\text{dyne},$$

and

$$\pi_{1212} = - 6.061 \times 10^{-14} \text{ cm}^2/\text{dyne}. \quad (6.3.18)$$

DISTRIBUTION LIST

This report is distributed as follows:

- 1) One original plus 50 copies to Army Research Office, Research Triangle Park.
- 2) 1 copy to Dr. C.S. Hartley, University of Alabama, Birmingham.
- 3) 1 copy to Dr. J. Prater, Army Research Office, Research Triangle Park.